Modelling of photonic crystal fibres

Bergbäck Knudsen, Erik; Bjarklev, Anders Overgaard; Broeng, Jes

Publication date:
2003

Document Version
Publisher's PDF, also known as Version of record

Modelling of Photonic Crystal Fibres

Erik Knudsen

February 28th 2003
revised: January 20th 2005

Supervisors:
Prof. Dr. Techn. Anders Bjarklev,
Ph.D. Jes Broeng.

Research Center COM
Technical University of Denmark
Building 345V
2800 Kgs. Lyngby
DENMARK

Abstract

In the present Ph.D.-work a theoretical study of aspects of modelling photonic crystal fibres was carried out. Photonic crystal fibres form a class of optical waveguides where guidance is no longer provided by a difference in refractive index between core and cladding. Instead, guidance is provided by an arrangement of air-holes running along the length of the fibre. Depending on the geometry of the fibre, the guiding mechanism may be either arising from the formation of a photonic bandgap in the cladding structure (photonic bandgap fibre), or by an effect resembling total internal reflection, which may described by an effective refractive index which is lower in the cladding than in the core (index guiding fibre).

By solving Maxwell's equations, under the conditions defined by the geometry of the fibre structure, we may predict the properties of the fibre. In all but rare cases, this is done via an approximative numerical modelling scheme. In this thesis, we describe some of the modelling procedures that have been proposed, with strong emphasis on the localised function method, and propose a novel variant of the former, which may overcome some of the shortcomings of the standard method. We give a detailed description of the new variant — the Hermite-Gaussian method. Hereafter, we model a range of photonic crystal fibres, including both index guiding and photonic bandgap fibres, using the Hermite-Gaussian method, and evaluate the results in view of the limitations inherent in the modelling procedure. We present modelling results for triangular and square lattice fibres, a novel pentagonal symmetric index guiding fibre, as well as a honeycomb bandgap fibre and the first analysis of semi-periodic layered air-hole fibres.

Using the modelling framework established as a basis, we provide an analysis of microbend loss, by regarding displacement of a fibre core as a stationary stochastic process, inducing mismatch between modes in contiguous fibre segments curved at different radii. Overall microbend loss is expressed as a statistical mean of mismatch losses.

Extending a well proven, established formula for macrobending losses in step index fibres, we provide an estimate of macrobend losses in an air-guiding photonic bandgap fibre, based on effective refractive index arguments.

Sammenfatning

I dette Ph.D.-projekt er udført en teoretisk studie over nogle aspekter af modellering af fotoniske krystalfibre. Fotoniske krystalfibre danner en klasse af optisk bølgeledere, hvis bølgeledning ikke afhænger af en forskel i brydningsindeks mellem kerne og kappe. I stedet føres de elektromagnetiske bølger gennem fiberen af et arrangement af luftcylindere på langs af fiberen. Afhængig af geometrien i fiberen, kan den ledende mekanisme opstå som følge af den fotoniske båndgabseffekt (eng. photonic bandgap effect) (båndgabsfiber), eller som en følge af at lufthullerne sænker det gennemsnitlige brydningdindeks i kappen (indeksførende fiber), hvilket kan modelleres ved at indføre et effektivt refraktivt indeks.

Vha. løsninger til Maxwells ligninger under de randbetingelser som fiberens geometri stipulerer, er det muligt at forudsige egenskaber hos den enkelte fiber. I de fleste tilfælde er dette kun muligt numerisk, vha. en approksimativ løsningsmetode. I denne afhandling beskrives, kortfattet, nogle af de løsningsmetoder der hidtil er blevet foreslået i litteraturen, med tyngdepunkt på den lokaliserede funktionsmetode. (eng. localised function method) Herudover præsenteres, i detalje, en ny variant af denne metode, Hermite-Gauss-metoden, der har til formål, at overkomme nogle af ulemperne ved den lokaliserede funktionsmetode. Den nye metode anvendes på en bred vifte af fotoniske krystalfibre, indeksførende, såvel som båndgabsfibre. I første omgang på kendte eksempler, for at afprøve grænserne for metodens muligheder, herunder præsenterer vi modelleringsresultater for triangulære og kvadratiske indeksførende fibre samt for en honeycomb-båndgabsstruktur, og derefter på nye fiberstrukturer for finde løsninger som ikke er mulige med andre metoder. De nye fiberstrukturer inkluderer en pentagonal indeksførende fiber og to forskellige semiperiodiske, luft-kernebåndgabsfibre.

Med det udviklede modelleringsværktøj som basis, udfører vi en analyse af mikrobøjningstab. Her betragter vi en lateral forflytning, og dermed bøjningsradius, af fiberkernen som en stationær stokastisk proces. Dette fører til en fejltilpasning mellem elektromagnetiske felter i fibersegment med forskellige bøjningsradier. Det totale mikrobøjningstab kan derefter skrives som en statistisk middelværdi af tilpasningstab.

I en afsluttende del af afhandlingen udbygges en velkendt formel for makrobøjningstab, til at omfatte en fotonisk båndgabsfiber med hul kerne, hvor analysen baseres på betragtninger af effektive brydningsindeks.

Contents

Chapter 1

Introduction

Since their inception, optical fibres have been used for a wide variety of applications. Strictly speaking, an optical fibre is a transmission line for optically carried signals, analogous to electrical transmission lines. The concept of transmitting signals at optical frequencies instead of electrical is certainly appealing, due to their inherently higher carrier frequencies. In light of this, the natural application of optical fibres is in the pure transmission industry, where they have so far been widely deployed [1]. Optical fibres do, however have many other interesting features that may be exploited. Numerous examples may be found in sensory applications, where optical fibre sensors have been used in diverse applications: as gyroscopes [2], naval hydrophones [3], chemical mixture sensors in oil/gas wells [4], structural integrity sensors in buildings [5], and many others [6].

Standard optical fibres generally consist of a fibre core, with a higher refractive index than the surrounding material – the cladding. The difference in refractive index is induced by selectively introducing dopants in the background material. Since the availability of low-loss pure silica is comparatively high, most fibres today are made in a silica-germanium system (with Ge. as the dopant raising the refractive index), but other material systems are used (for instance sapphire [7]), especially for wavelengths outside the visible and near-infrared ranges. Dopants introduce scattering losses. Hence, the concentrations must be kept at a minimum. A high refractive index contrast on the other hand, leads to better field confinement in the fibre, which, in turn, helps in avoiding such generally unwanted effects as bending loss. This tradeoff is in general balanced such that the refractive index contrast is approximately 1% [1].

1.1 Photonic crystals

A photonic bandgap is a frequency range in which photons are not allowed to propagate in certain directions (stop band), in analogy with the electronic bandgaps found in semiconductors, where electrons are disallowed from certain energy ranges [8]. Electronic bandgaps arise from the periodic variations of the atomic potential in a crystal, whereas a photonic bandgap must be artificially introduced, by micro-manufacturing periodic changes in the refractive index potential. The periodicity of the crystal must be of the same order as the wavelength of the photons. Hence, very strict demands on manufacturing tolerances are imposed when realising

photonic bandgap structures.

Photonic bandgap structures, or photonic crystals [9], were proposed by Yablonovitch and John in 1987 [10] [11], and are, with the rapidly improving micro-manufacturing techniques, fuelled by the semiconductor industry [12] (in an integrated optics context) and the telecommunications industry (in a fibre context), becoming more and more technologically feasible. 3-dimensional photonic bandgaps have been observed, and experimentally verified in the microwave and optical ranges, in a number of different structures, such as the Yablonovite [13], the inverted opal [14] [15], or the log-pile structure [16] [17][1]. In this light, the vision of furthering the semiconductor analogy into making optical components with properties analogous to those in integrated electronics, has been put forward as a way of revolutionising the field of photonics as semiconductors have done electronics [18].

1.2 Photonic crystal fibres

The terms *photonic bandgap* and *photonic crystal*, although originally coined on structures exhibiting full, 3-dimensional stop bands, has also been adopted for structures in only 2-dimensions. In these structures complete bandgaps do not exist for all directions, and not necessarily for both polarisations of the light. Consider, for instance, an arrangement of parallel dielectric rods, prolonged into infinity (fig. 1.1(a)), where the rods are situated on the lattice sites of a square lattice [18]. This structure may exhibit a 2-dimensional photonic bandgap in the plane perpendicular to the rods, provided that the refractive index contrast between the rods and the surrounding material is sufficiently large. I.e. photons in a certain frequency range may not propagate perpendicular to the rods. The inverse of this structure may also exhibit a bandgap, if the index contrast is sufficient. A triangular lattice of air-cylinders (fig. 1.1(b)) in a silica background does not exhibit a bandgap per se. It has, however, been shown that bandgaps "open up" when the photons' frequency components parallel to the cylinders, rise above a certain level [19].

Again, in analogy with semiconductor bandgaps, photonic bandgaps become ever more useful when defects are introduced into the perfect

[1] The inverted opal may be considered of particular interest since the artificial opal, on which it is based, is a self-organising system

crystal. Thus, we may for instance create line defects, along which photons may travel, or point defects (fig. 1.1(c)) amounting to micro-cavities. In a 2-dimensional sense, a point defect may be created by removing one of the rods (or cylinders). A photon with a frequency in the bandgap may travel along the defect, but is restricted from entering the surrounding structure by the bandgap. Thus, a Photonic crystal optical fibre[2] (PCF) is created, whose core is a 2-d "point" defect and whose cladding consists of the periodic lattice structure. There are no fundamental requirements on the nature of the defect, as long as it introduces an energy state within the photonic bandgap. This includes the possibility of a low index defect, yielding the unique opportunity of creating an optical fibre, which guides light in an air-core [20]. Because of the fundamentally different light-guiding principle, photonic bandgap fibres have, in many respects, very different characteristics than conventional fibres [21] [22] [23].

A photonic crystal fibre with a triangular lattice structure may be realised by stacking capillary tubes in a hexagonal pattern, replacing one or more tubes to create a defect. The whole arrangement may then be drawn into a fibre using conventional fibre drawing facilities. Generally the gaps in such a fibre are narrow, depending on the size of the capillary tubes. Stacking capillary tubes in a honeycomb pattern yields a structure with wider bandgaps, hence the structure is less sensitive to crystal imperfections [24].

As mentioned, the periodicity of the cladding structure is on the same order as the operating wavelength. Due to this fact a second kind of photonic crystal fibre has been intensively studied, namely the index guiding photonic crystal fibre. This kind of fibre does not rely on photonic bandgaps at all in order to guide light, instead guidance is provided by the existence of an effective index contrast between core and cladding. The core, defined by a "crystal defect" must have a higher index than the elements forming the crystal. This might be effectuated in a triangular lattice silica air system, by replacing one or more of the capillary tubes by a solid silica rod. The effective index of the cladding is bounded by the background material index and the index of the crystal elements, but varies strongly with wavelength [25] [26] [27]. Manufacturing tolerances for this kind of fibre are significantly relaxed compared to photonic

[2] Other names found in the literature are microstructured optical fibre and holey fibre.

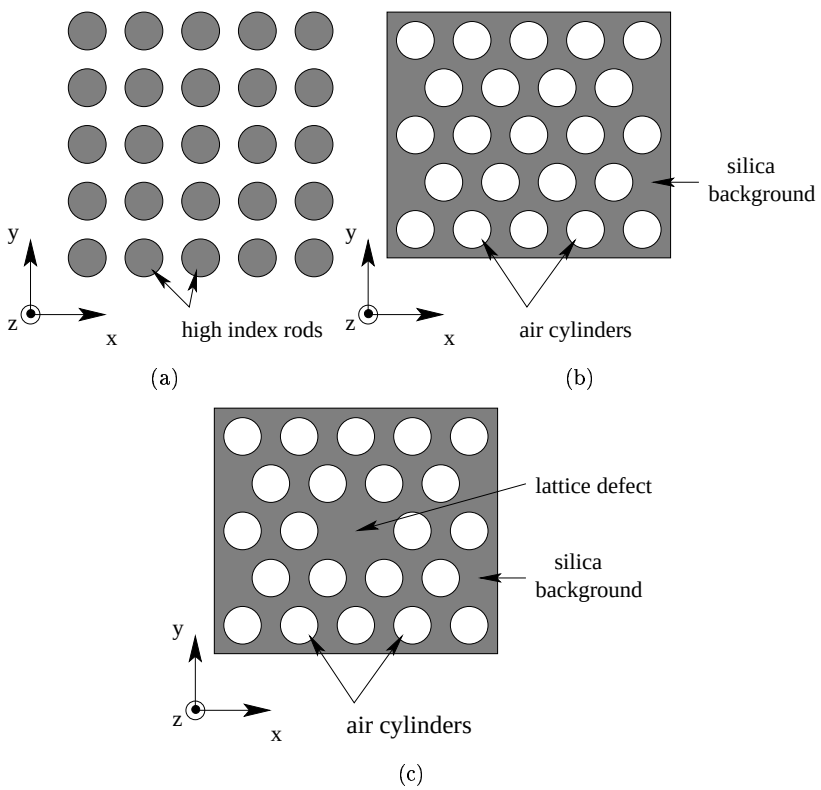

Figure 1.1: 2d-photonic crystal structures: Quadratic lattice arrangement of rods (a). Triangular lattice cladding structure (b). Triangular structure with defect forming a fibre core (c).

bandgap fibres. The guiding principles in index guiding fibres are similar to conventional fibres — nevertheless they exhibit many features not present in conventional fibre technology. In a telecommunications context, the dispersion characteristics of index guiding PCFs are highly different and may be tailored by proper fibre design [28]. As an example, a zero-dispersion wavelength $< 1.3\mu m$ is possible. Also, the lack of dopants in the fibre, yields a possibility of high confinement, as a result of a high effective index contrast, whilst retaining low scattering losses. For other applications, both photonic bandgap PCFs as well as index guiding PCFs may be used to force an interaction between a material injected into the voids of the crystal and the electromagnetic fields propagating through the fibre. It is also conceivable to construct highly birefringent fibres by introducing asymmetries in either core or cladding. This may be done by altering the structure of the cladding or core [29] [30].

1.3 Modelling

To predict the properties of a particular photonic crystal fibre, it is necessary to solve Maxwell's equations under conditions specified by the geometry of the fibre. In a few special cases it is possible to obtain analytic, closed form solutions [25] [31], but in general some numeric, approximative scheme must be employed. Many different modelling schemes have so far been suggested, each with their own strengths and weaknesses. The most widely used method is probably the plane wave method [32] [33], which relies on a Fourier expansion of the dielectric function, and electromagnetic field solutions in terms of Bloch states, thus utilising the periodicity of the underlying structure. Others methods include the finite element method [34], which, although being an established and proven method in many fields of science, has the disadvantage that it is computationally very intensive, and the multipole method, developed by White et. al. [35] [36], relying on a series expansion of the electromagnetic fields in terms of cylindrical harmonics. The multipole method has the pleasing features that it enables exact enforcement of boundary conditions and possible inclusion of leakage loss [37].

In order To scale down computational demands, the idea of using localised functions, in analogy to wavelets [38], has been suggested [39] [40] [41] [42]. When using the standard Hermite Gaussian localised function

methods, the refractive index of the cladding structure is expanded into a Fourier series, whereas the electromagnetic fields (and possibly the refractive index of the core), are expanded into series of two-dimensional Hermite Gaussian functions. This facilitates efficient modelling of defect modes at the expense of an accurate cladding mode description. A drawback of these methods is that it is not possible to model finite structures. We propose a variant of the localised function method, where the electromagnetic fields as well as each air-hole in the cladding is expanded locally into a series of Hermite Gaussian functions. The general photonic crystal structure is then composed by a superposition of several, localised series expansions.

1.4 Outline of thesis

The remainder of the thesis is organised as follows: Chapter 2 describes the theoretical framework of Hermite Gaussian-series based localised functions methods, existing versions briefly, the new modelling scheme we propose, in detail. Firstly the common ground of the modelling schemes is established, where the Maxwellian wave-equations are transformed into an operator matrix eigenvalue problem. Thereafter we derive the elements of the operator matrix particular to the new formulation which, as noted, is constructed from superpositions of localised basis expansions. The chapter ends with a description of some key formulae of fibre optics, in a form greatly simplified by the formulation in terms of Hermite Gaussian functions.

In Chapter 3 we use the new modelling scheme from the preceding chapter to predict features of several PCFs, ranging from the simple triangular lattice structure through other index guiding fibres to photonic bandgap fibres (honeycomb and semi-periodic layered structures), in terms of field distributions, mode effective area etc. This will serve to showcase the versatility and illustrate the shortcomings of the localised functions model. The section on modelling honeycomb and semi-periodic layered fibres (colloquially referred to as "onion" fibres) presented in the end of chapter 3 presents an attempt at modelling bandgap fibres with localised functions although they are clearly not suited for the task.

Chapter 4 is devoted to an application oriented aspect of fibre technology, microbend induced losses. A real fibre is not perfectly straight

after draw — instead it will exhibit small fluctuations around a mean centreline, and, hence, will suffer from microbending losses. In this chapter we present an extension to the localised functions method described in earlier chapters, enabling us to evaluate the effect of microbends from a statistical viewpoint. This approach is highly justified by the stochastic nature of micro-bends.

Chapter 5 presents a return to a known modelling scheme, the plane wave method, in order provide an estimate of macrobending losses in an air-guiding PCF. The magnitude of macrobending loss depends highly on the field amplitudes in the cladding. As the shortcomings of the localised function method include an inability to accurately describe the electromagnetic fields in the cladding of a fibre, the decision was in favour of the plane wave method. A well known formula is applied with modifications to evaluate the overall bending loss of the fibre.

Chapter 6 holds some concluding remarks on the work described in this thesis.

References to chapter 1

[1] G. P. Agrawal. *Fiber-optic communication systems.* John Wiley and sons Inc., Third edition, 2002.

[2] R. A. Bergh, H. C. Lefevre, and H. J. Shaw. "An overview of fiber-optic gyroscopes", *Journal of Lightwave Technology*, vol. 2, no. 2, pp. 91–107, 1984.

[3] S. Takahashi, T. Kikuchi, R. Yagi, and A. Hasegawa. "A single fiber heterodyne optical fiber hydrophone", *Japanese Journal of Applied Physics: Supplement*, vol. 27, pp. 91–93, 1988.

[4] M. Eriksrud and H. Nakstad. "An optical fibre instrumentation system for pressure and temperature measurement in oil and gas well — from design to installation and operation", in *Conference on Lasers and Electro-Optics, Europe,* p. 240, 1998.

[5] M. Maalej and S. H. Rizkalla. "Fibre optic sensing and intelligent processing of sensor data for structural health monitoring", in *OFS200, 14th International Conference on Optical Fibre Sensors,* 2000.

[6] T. G. Giallorenzi, J. A. Bucaro, G. H. J. Dandridge, J. H. Cole, S. C. Rashleigh, and R. G. Priest. "Optical fibre sensor technology", *Journal of Quantum Electronics*, vol. 18, no. 4, pp. 626–665, 1982.

[7] I. D. Aggarwal and J. S. Sanghera, editors. *Infrared fiber optics*. CRC Press, 1998.

[8] B. G. Streetman. *Solid state electronic devices*. Prentice Hall, 1995.

[9] K. Okanoda. *Optical properties of photonic crystals*. Springer Verlag, 2001.

[10] E. Yablonovitch. "Inhibited spontaneous emission in solid-state physics and electronics", *Physical Review Letters*, vol. 58, no. 20, pp. 2059–2062, 1987.

[11] S. John. "Strong localization of photons in certain disordered superlattices", *Physical Review Letters*, vol. 58, no. 23, pp. 2486–2489, 1987.

[12] K. Goser. *Großintegrationstechnik*. Hüthig Verlag, 1991.

[13] E. Yablonovitch. "Photonic band-gap structures", *Journal of the Optical Society of America*, vol. 10, no. 2, pp. 283–295, 1993.

[14] K. Busch and S. John. "Photonic band gap formation in certain self-organizing systems", *Physical Review E*, vol. 58, no. 3, pp. 3896–3908, 1998.

[15] S. John and K. Bursch. "Photonic band gap formation and tunability in certain self-organizing systems", *Journal of Lightwave Technology*, vol. 17, no. 11, pp. 1931–1943, 1999.

[16] S. Noda, K. Tomoda, and A. Yamamoto, N. Chutinan. "Full three-dimensional photonic bandgap crystals at near-infrared wavelengths", *Science*, vol. 289, no. 5479, pp. 604–606, 2000.

[17] M. Bayindir, G. Temelkuran, and E. Ozbay. "Propagation of photons by hopping: A waveguiding mechanism through localized cuoled cavities in three-dimensional photonic crystals", *Physical Review B*, vol. 61, no. 18, pp. R11855–R11858, 2000.

[18] J. D. Joannopoulos, R. D. Meade, and J. N. Winn. *Molding the flow of light*. Princeton University Press, 1995.

[19] T. A. Birks, P. J. Roberts, P. S. Russell, D. M. Atkin, and T. J. Shepherd. "Full 2-d photonic badngaps in silica/air structures", *EL*, vol. 31, no. 22, pp. 1941–1943, 1995.

[20] R. F. Cregan, B. J. Mangan, J. C. Knight, T. A. Birks, P. J. Russell, P. St.J. Roberts, and D. C. Allan. "Single-mode photonic band gap guidance of light in air.", *Science*, vol. 285, no. 5433, pp. 1537–1539, 1999.

[21] J. Broeng, S. E. Barkou, A. Bjarklev, and T. Søndergaard. "Analysis of air-guiding photonic bandgap fibers", *Optics Letters*, vol. 25, no. 2, pp. 96–98, 2000.

[22] A. Bjarklev, J. Broeng, S. E. Barkou, and T. Søndergaard. "Fundamentally new microstructured fiber waveguides for potential sensor applications", in *Light for Life, Cancun, Mexico,* 1999.

[23] E. Knudsen, A. Bjarklev, J. Broeng, and S. E. Barkou. "Macrobending loss estimation for air-guiding photonic crystal fibers", in *OFS200, 14th International Conference on Optical Fibre Sensors,* 2000.

[24] S. E. Barkou, J. Broeng, and A. Bjarklev. "Silica-air photonic crystal fiber that permits waveguiding by a true photonic bandgap effect", *Optics Letters*, vol. 24, no. 1, pp. 46–48, 1999.

[25] T. J. Shepherd, P. J. Roberts, and R. Loudon. "Soluble two-dimensional photonic crystal model", *Physical Review E*, vol. 55, no. 5, pp. 6024–6038, 1997.

[26] T. A. Birks, D. Mogilevtsev, J. C. Knight, P. S. Russel, J. Broeng, P. J. Roberts, J. A. West, D. C. Allan, and J. C. Fajardo. "The analogy between photonic crystal fibres and step index fibres", in *OFC/IOOC'99, volume 4,* pp. 114–116, 1999.

[27] T. M. Monro, D. A. Richardson, and P. J. Bennett. "Developing holey fibres for evanescent field devices", *EL*, vol. 35, no. 14, pp. 1188–1189, 1999.

[28] F. A., E. Silvestre, J. J. Andres, P. Miret, and A. M. V. "Designing th eproperties of dispersion flattened photonic crystal fibers", *Optics Express*, vol. 9, no. 13, pp. 687–697, 2001.

[29] M. J. Steel and R. M. Osgood. "Elliptical-hole photonic crystal fibers", *Optics Letters*, vol. 26, no. 4, pp. 229–231, 2001.

[30] T. P. Hansen, J. Broeng, S. E. B. Libori, K. E., A. Bjarklev, J. J. R., and H. R. Simonsen. "Highly birefringent index-guiding photonic crystal fibers", *Photonics Technology Letters*, vol. 13, no. 6, pp. 588–590, 2001.

[31] M. Midrio, M. P. Singh, and C. G. Someda. "The space filling mode of holey fibers: An analytical solution", *Journal of Lightwave Technology*, vol. 18, no. 7, pp. 1031–1037, 2000.

[32] R. D. Meade, A. M. Rappe, K. D. Brommer, J. D. Joannopoulos, and O. L. Alerhand. "Accurate theoretical analysis of photonic band-gap materials", *Physical Review B*, vol. 48, no. 11, pp. 8434–8437, 1993.

[33] S. G. Johnson and J. D. Joannopoulos. "Block-iterative frequency domain methods for maxwell's equations in a planewave basis", *Optics Express*, vol. 8, no. 3, pp. 173–190, 2001.

[34] A. Peyrilloux, S. Février, J. Marcou, L. Berthelot, P. Pagnoux, and D. Sansonetti. "Comparison between the finite element method, the localised function method and a novel equivalent averaged index method for modelling photonic crystal fibres", *Journal of Optics: Pure and Applied Optics*, vol. 4, no. 3, pp. 257–262, 2002.

[35] T. P. White, B. T. Kuhlmey, R. C. McPhedran, D. Maystre, G. Renversez, C. M. de Sterke, and L. C. Botten. "Multipole method for microstructured optical fibers. i. formulation", *Journal of the Optical Society of America B*, vol. 19, no. 10, pp. 2322–2330, 2002.

[36] B. T. Kuhlmey, T. P. White, G. Renversez, D. Maystre, L. C. Botten, C. M. de Sterke, and R. C. McPhedran. "Multipole method for microstructured optical fibers. ii. implementation and results", *Journal of the Optical Society of America B*, vol. 19, no. 10, pp. 2331–2440, 2002.

[37] T. P. White, R. C. McPhedran, C. M. de Sterke, L. J. Botten, and M. J. Steel. "Confinement losses in microstructured optical fibers", *Optics Letters*, vol. 26, no. 21, pp. 1660–1662, 2001.

[38] A. Graps. "An introduction to wavelets", *IEEE Computational Science and Engineering*, vol. 2, no. 2, pp. 50–61, 1995.

[39] D. Mogilevtsev, T. A. Birks, and P. S. Russel. "Group velocity dispersion in photonic crystal fibers", *Optics Letters*, vol. 23, no. 21, pp. 1662–1664, 1998.

[40] T. M. Monro, D. J. Richardson, N. G. R. Broderick, and P. J. Bennett. "Holey optical fibers. an efficient modal model", *Journal of Lightwave Technology*, vol. 17, no. 11, pp. 2078–2081, 1999.

[41] D. Mogilevtsev, T. A. Birks, and P. S. Russel. "Localized function method for modeling defect modes in 2-d photonic crystals", *Journal of Lightwave Technology*, vol. 17, no. 11, pp. 2078–2081, 1999.

[42] J. P. Albert, C. Jouanin, D. Cassagne, and D. Bertho. "Generalized wannier function method for photonic crystals", *Physical Review B*, vol. 61, no. 7, pp. 4381–4384, 2000.

Chapter 2

Theoretical framework

2.1 Localised functions in general

A practically useful optical waveguide must have its power distribution concentrated to the core region. For some applications a large core area may be wanted - for others a high intensity is the target, but in both cases, the electromagnetic field distribution is in some sense localised. It is therefore reasonable to to express the field solutions to Maxwell's equations in terms of functions that are localised around this core region. The simplicity of a Fourier-series[1] may be lost, but if this loss may be regained, in terms of calculation efficiency, or resolution in targeted regions, it may be well worth the effort. This train of thought is also the main argument behind the whole field of wavelet study, i.e. to describe a phenomenon using a set of functions which shows fine resolution around points of interest while not wasting resources of resolution elsewhere, where it is not needed. In the fibre case, the area of interest is usually the core region - whereas areas far into the cladding may be of little interest. Also, any real fibre will infallibly have imperfections, such as bends, which deform the outer ends of the fields, rendering an ideal description inaccurate in any case.

In the same way as there are multiple classes of wavelets, [1] [2] several sets of functions have been suggested for this kind of localised expansion [3] [4] [5]. It may be remarked, that although the term is rather general, the modelling scheme usually referred to as *the* Localised Function Method [4] [5], is based on expansion series in terms of Hermite polynomials.

Generally PCFs are of a periodic nature. This is partly due to their origin in the notion of the photonic bandgap, and partly because of the established manufacturing technique being a "stack-and-draw" procedure, where glass (or indeed any other material that may be drawn into a fibre) tubes are stacked, fused together, and thereafter drawn into a fibre using conventional drawing facilities. PCFs operating by the photonic bandgap effect do need a periodic cladding (or semi-periodic[2] [6]), whereas index-guiding PCFs may even have a random distribution of low index material [7]. Considering the periodicity of the structure we may take advantage of Bloch's theorem [8] in describing the electromagnetic fields. This is the starting point of the so called plane wave method [9] [10], which relies on

[1] Generally the first choice for any series expansion

[2] Such as having cylinders on the nodes of a Penrose tiling

a Fourier formulation of the wave equations. To avoid infinite expansion series, periodical field distributions must be forced. When using the plane wave method this is achieved via a supercell approximation, i.e. the field distribution as well as the dielectric function is repeated indefinitely. If the supercell is chosen to be large enough results will be accurate, but the calculation effort scales with increasing supercell size.

Albert et.al. [3] [11] have proposed a method in which localisation is taken advantage of, by letting a lattice structure be described by Bloch's theorem, but instead of enforcing a supercell to contain the electromagnetic field distribution, it is described by generalised Wannier-functions.

The use of Hermite Gaussian series to express electromagnetic modes in fibre optics is a natural choice, considering the fact that the modes of an infinitely parabolic optical fibre are Hermite Gaussian [12]. Hermite Gaussian functions (eq. 2.6) form a complete orthogonal set and so may be used as a general basis for a series expansion to approximate any function. Because of their Gaussian nature, however, they are impractical for resolving function features far away from the function series origin. The orthogonality of the function set is helpful in the direct transformation into a matrix eigenvalue-problem, as it removes the need for a diagonalisation and following inversion of one matrix of the same size as the eigenvalue problem. Another reason for using Hermite polynomials to form a basis of L^2 is that they are particularly simple to differentiate (eq. 2.20). To use only Hermite Gaussian series centred around a waveguide core, appealing as the thought may be, is not practical for realisable microstructured waveguides since the low leakage loss operation generally requires a cladding structure of an extent exceeding the limit of practical use for the series.

To counter this, Mogilevtsev et.al. [4] and Monro et.al. [5] have suggested using a combination of Fourier and Hermite Gaussian expansion series to exploit the "best of both worlds". This has proven to be an efficient and practical modelling scheme, although it requires that the dielectric structure is somehow approximated by a periodic structure. Drawing on ideas from quantum mechanics, we propose that the interaction between the electromagnetic fields and the dielectric structure be expressed as a superposition of the interaction between the fields and a number of defects in a background material. In principle, the defects may be of any shape, although PCFs are generally manufactured to have circular air-holes in a

silica background[3] (fig. 2.6).

2.2 Formulation of the eigenvalue problem

Assuming the fibre to be uniform in the z-direction (the direction of propagation), we may write the magnetic field[4] of the jth mode as [12]:

$$\boldsymbol{H}_j(x,y,z) = \left(\boldsymbol{h}_j^t(x,y) + h_j^z(x,y)\hat{\boldsymbol{z}}\right)\exp(j\beta_j z) \tag{2.1}$$

where $\boldsymbol{h}_j^t(x,y) = h_j^x\hat{\boldsymbol{x}} + h_j^y\hat{\boldsymbol{y}}$ is the transverse component of the magnetic field and h_j^z the longitudinal. Substituting eq. 2.1 into the full vector wave equation for magnetic fields, we get a pair of coupled wave equations:

$$\left(\nabla_t^2 + \epsilon k^2 - \beta_j^2\right) h_j^x = \left(\frac{\partial h_j^y}{\partial x} - \frac{\partial h_j^x}{\partial y}\right)\left(\frac{\partial \ln(\epsilon)}{\partial y}\right) \tag{2.2}$$

$$\left(\nabla_t^2 + \epsilon k^2 - \beta_j^2\right) h_j^y = \left(\frac{\partial h_j^x}{\partial y} - \frac{\partial h_j^y}{\partial x}\right)\left(\frac{\partial \ln(\epsilon)}{\partial x}\right) \tag{2.3}$$

where ∇_t^2 is the transverse Laplacian operator and $\epsilon = \epsilon(x,y)$ is the dielectric function of the structure considered. We now consider the following series expansion of the transverse magnetic field:

$$\boldsymbol{h}_j^t = \sum_{a,b=0}^{F} \mathcal{H}_{ab}^x \psi_{a,b}^{\omega_m}(x,y)\hat{\boldsymbol{x}} + \mathcal{H}_{ab}^y \psi_{a,b}^{\omega_m}(x,y)\hat{\boldsymbol{y}} \tag{2.4}$$

Here the subscript m has been used to differentiate ω_m of the field expansion series, from the structure characteristic width, ω_d, which will be discussed later.

The Hermite Gaussian functions are defined as:

$$\psi_{a,b}^{\omega}(x,y) = \psi_a^{\omega}(x)\,\psi_b^{\omega}(y) \tag{2.5}$$

$$\psi_a^{\omega}(x) = \frac{2^{-\frac{a}{2}}\,\pi^{-\frac{1}{4}}}{\sqrt{a!\,\omega}}\,e^{-\frac{x^2}{2\omega^2}}H_a(\frac{x}{\omega}) \tag{2.6}$$

[3] Other shapes of holes tend to become circular during draw, due to surface tension.

[4] We have chosen to solve the wave equations for the magnetic field, since it yields a slightly simpler structure of the calculations later on.

where H_a denotes the Hermite polynomial of order a (eq. 2.7). The parameter ω is a characteristic width parameter of the functions.

$$H_a = (-1)^n e^{x^2} \frac{d^a}{dx^a}\left(e^{-x^2}\right) \tag{2.7}$$

Differentiating Hermite Gaussian functions of this form is a simple operation using the recursion formulae for Hermite polynomials (eqs. 2.20 and 2.21). As noted above, this function series forms an orthogonal set. Specifically the Hermite polynomials are orthogonal with respect to the weight function e^{-x^2}. I.e.:

$$\int_{\mathbb{R}} e^{-x^2} H_a(x) H_b(x) \mathrm{d}x = \begin{cases} \frac{2^{-a}}{\sqrt{\pi a!}}; & a = b \\ 0; & a \neq b \end{cases} \tag{2.8}$$

If we substitute eq. 2.4 into eqs. 2.2 and 2.3, multiply by $\psi_{c,d}^{\omega_m}(x,y)$ and perform overlap integrals over the infinite cross-section, we, by orthogonality, directly get an eigenvalue problem of the following form[5].

$$\mathbf{M}\boldsymbol{\mathcal{H}} = \frac{\beta^2}{k^2}\boldsymbol{\mathcal{H}} \tag{2.9}$$

where the eigenvectors to be solved for, are the expansion coefficients of the modal fields and the eigenvalues are the modal indices, or propagation factors, of the associated wave solution.

$$\boldsymbol{\mathcal{H}} = \begin{pmatrix} \mathcal{H}_{00}^x \\ \mathcal{H}_{01}^x \\ \vdots \\ \mathcal{H}_{FF}^x \\ \mathcal{H}_{00}^y \\ \vdots \\ \mathcal{H}_{FF}^y \end{pmatrix} \tag{2.10}$$

[5] Had the functions not been orthonormal, the right hand side of eq. 2.9 would have read: $\mathbf{M}\boldsymbol{\mathcal{H}} = \frac{\beta^2}{k^2}\mathbf{S}\boldsymbol{\mathcal{H}}$ To arrive at eq. 2.9 we would have to diagonalise $\mathbf{S}$, i.e. calculate its eigenvectors, and perform an additional matrix inversion. Although it has yet to be shown, this procedure may in some cases be preferable, if the set of basis functions and its corresponding set of overlap integrals, are sufficiently simple and numerically stable.

The matrix, $\boldsymbol{M}$, of the eigenvalue problem is a $2(F+1)^2 \times 2(F+1)^2$ matrix

$$\boldsymbol{M} = \begin{pmatrix} \boldsymbol{M}^{xx} & \boldsymbol{M}^{xy} \\ \boldsymbol{M}^{yx} & \boldsymbol{M}^{yy} \end{pmatrix};\ \boldsymbol{M}^{sp} = \begin{pmatrix} M^{sp}_{0000} & \dots & M^{sp}_{00FF} \\ \dots & \dots & \dots \\ M^{sp}_{FF00} & \dots & M^{sp}_{FFFF} \end{pmatrix} \tag{2.11}$$
$$s,p \in \{x,y\};\ s \neq p$$

with matrix elements given by sums of overlap integrals:

$$\begin{aligned} M^{ss}_{abcd} &= \frac{1}{k^2} I^{(1)}_{abcd}(\omega_m) + I^{(2)}_{abcd}(\omega_m) + \frac{1}{k^2} I^{(3)ss}_{abcd}(\omega_m) \\ M^{sp}_{abcd} &= -\frac{1}{k^2} I^{(3)sp}_{abcd}(\omega_m) \\ & s,p \in \{x,y\} \end{aligned} \tag{2.12}$$

where the uncoupled terms, $I^{(1)}_{abcd}$, $I^{(2)}_{abcd}$ and $I^{(3)ss}_{abcd}$, are given by:

$$I^{(1)}_{abcd}(\omega_m) = \iint_{\mathbb{R}^2} \psi^{\omega_m}_c(x)\psi^{\omega_m}_d(y)\,\nabla^2\left[\psi^{\omega_m}_a(x)\psi^{\omega_m}_b(x)\right]\mathrm{d}x\mathrm{d}y \tag{2.13}$$

$$I^{(2)}_{abcd}(\omega_m) = \iint_{\mathbb{R}^2} \psi^{\omega_m}_a(x)\psi^{\omega_m}_c(x)\psi^{\omega_m}_b(y)\psi^{\omega_m}_d(y)\,\epsilon(x,y)\ \mathrm{d}x\mathrm{d}y \tag{2.14}$$

and

$$I^{(3)xx}_{abcd}(\omega_m) = \iint_{\mathbb{R}^2} \psi^{\omega_m}_a(x)\psi^{\omega_m}_c(x)\frac{\partial\psi^{\omega_m}_b(y)}{\partial y}\psi^{\omega_m}_d(y)\frac{\partial \ln\left(\epsilon(x,y)\right)}{\partial y}\mathrm{d}x\mathrm{d}y \tag{2.15}$$

$$I^{(3)yy}_{abcd}(\omega_m) = \iint_{\mathbb{R}^2} \frac{\partial\psi^{\omega_m}_a(x)}{\partial x}\psi^{\omega_m}_c(x)\psi^{\omega_m}_b(y)\psi^{\omega_m}_d(y)\frac{\partial \ln\left(\epsilon(x,y)\right)}{\partial x}\mathrm{d}x\mathrm{d}y \tag{2.16}$$

and the coupling terms, $I^{(3)sp}_{abcd}$, by:

$$I^{(3)xy}_{abcd}(\omega_m) = \iint_{\mathbb{R}^2} \frac{\partial \psi^{\omega_m}_a(x)}{\partial x} \psi^{\omega_m}_c(x) \psi^{\omega_m}_b(y) \psi^{\omega_m}_d(y) \frac{\partial \ln(\epsilon(x,y))}{\partial y} \mathrm{d}x\mathrm{d}y \tag{2.17}$$

$$I^{(3)yx}_{abcd}(\omega_m) = \iint_{\mathbb{R}^2} \psi^{\omega_m}_a(x) \psi^{\omega_m}_c(x) \frac{\partial \psi^{\omega_m}_b(y)}{\partial y} \psi^{\omega_m}_d(y) \frac{\partial \ln(\epsilon(x,y))}{\partial x} \mathrm{d}x\mathrm{d}y \tag{2.18}$$

2.3 The dielectric function.

The overlap integrals $I^{(2)}$ and $I^{(3)sp}; s, p \in \{x, y\}$ express the interaction between the electromagnetic fields and the dielectric medium. In order to quantify this interaction we need to find a suitable, practical description of the dielectric function. The most straightforward way of doing that would be to simply integrate numerically over an infinite cross-section. If the number of objects is small this may indeed be efficient and accurate. For larger numbers of holes, however, it could pose a difficult numerical problem, considering the often discontinuous nature of the dielectric function (such as air objects in a glass background). We may instead use a series expansion to express the dielectric. For symmetry reasons a direct expansion into a Hermite Gaussian series might seem reasonable[6]. As noted above, a practical photonic crystal, however, needs to be of some lattice periods (or in a non-lattice sense, the arrangement of low-index objects must be large enough to create an efficient low-index barrier), extent in order to keep leakage loss at a reasonable level [13], which makes this rather impractical. For this reason, especially considering the periodic nature of most photonic crystal fibres, a Fourier expansion is more adequate.

[6]This would yield a very practical structure of the overlap integrals in eqs. 2.14 through 2.18. cf. sec. 2.3.2

2.3.1 Hybrid methods

Thus far, the Hermite Gaussian based localised function methods considered in the literature [4] [5] [14] [15] have been based on hybrid expansion schemes, where the dielectric function is expanded into either a combination of localised functions and periodic exponentials or a purely periodic exponential (Fourier) series. Since cladding structures of photonic crystal fibres generally are of a periodic nature, this has been proven efficient. It is however, necessary to enforce periodicity of the dielectric function, either by repeating the overall structure indefinitely or by extending the cladding pattern into infinity. In many cases this is sufficient - and because of the simple structure of calculations based on these methods, the methods are widely used.

Consider using trigonometric functions to expand the periodic part of the dielectric function and cancel one or more features in it by selectively adding a Hermite Gaussian series. In the simplest case, a single air-hole will be cancelled to create a high-index core region. The structure considered this way will have an infinite cladding - hence it is applicable to fibres with many holes surrounding the core.

The dielectric function is expressed in the following form:

$$\epsilon(x,y) = \sum_{f,g=0}^{D_1} c_{f,g}^1 \cos\left(\frac{2\pi f x}{\Lambda}\right)\cos\left(\frac{2\pi g y}{\Lambda}\right) + \sum_{f,g}^{D_2} c_{f,g}^2 \psi_{f,g}^{\omega_d}(x,y) \quad (2.19)$$

where D_1 and D_2 are the numbers of decomposition functions used.

Substituting eq. 2.19 into 2.14 through 2.18 and making use of recursion formulae (eqs. 2.20 and 2.21) for Hermite Polynomials [16],

$$\frac{dH_a(x)}{dx} = 2aH_{a-1}(x) \quad (2.20)$$

$$H_{a+1}(x) = 2xH_a(x) - 2aH_{a-1}(x) \quad (2.21)$$

we get overlap integrals of the two forms

$$\hat{I} = \int_{-\infty}^{\infty} \psi_a^{\omega_m}(x)\psi_c^{\omega_m}(x)\psi_f^{\omega_d}(x)dx \quad (2.22)$$

and

$$\tilde{I} = \int_{-\infty}^{\infty} \psi_a^{\omega_m}(x)\psi_c^{\omega_m}(x)\cos\left(\frac{2\pi f x}{\Lambda}\right)dx \quad (2.23)$$

These integrals may be solved analytically, and we may now assemble the eigenvalue problem and solve for eigenvalues and eigenvectors.

When combining expansion series of different types and/or lengths one must take series mismatch into account. In analogy to the Gibbs' phenomenon in Fourier series, Hermite Gaussian series exhibit an oscillatory behaviour near discontinuities in the expanded function which may interfere with the Gibbs' phenomenon of the Fourier series[7]. Also notable is general mismatch of the function series, who fail to cancel each other completely (fig. 2.1). The Gibbs' phenomenon of the Fourier series may be efficiently suppressed through Lanczos' σ-factors [17] - the series mismatch, however, may not. This effectively limits the gain of extending the Fourier series without extending the Hermite Gaussian series.

Instead of creating the core region by way of cancellation, we may repeat a fibre structure, complete with core, and expand it in its entirety in a Fourier series[8]. In this way we may take full advantage of many highly optimised algorithms and software packages developed for the Fourier transform, at the same time avoiding any problems of mismatching function series. In this case the dielectric function may be expressed in Cartesian coordinates as[9]:

$$\epsilon(x,y) = \sum_{f,g=-D}^{D} c_{f,g} \exp\left(i\left(\xi f x + \zeta g y\right)\right) \tag{2.24}$$

where the constants ξ and ζ depend on the imposed periodicity of the structure.

Substituting eq. 2.24 into eqs. 2.14 through 2.18, and making use of recursion formulae (eqs. 2.20 and 2.21), we essentially get overlap integrals of the two forms

$$\hat{I} = \int_{-\infty}^{\infty} \psi_a^{\omega_m}(x)\psi_c^{\omega_m}(x) \cos\left(\frac{\xi f x}{\Lambda}\right) dx \tag{2.25}$$

and

$$\tilde{I} = \int_{-\infty}^{\infty} \psi_a^{\omega_m}(x)\psi_c^{\omega_m}(x) \sin\left(\frac{\zeta g x}{\Lambda}\right) dx \tag{2.26}$$

[7]The behaviour of the Gibbs' like phenomenon is dependent on the relative characteristic width of the series (fig. 2.3).

[8]This treatment of the dielectric function is the same as in the plane wave method.

[9]We may also take advantage of symmetries in the crystal structure, as is generally done with the plane wave method, and instead express the structure in terms of its reciprocal lattice vectors [18].

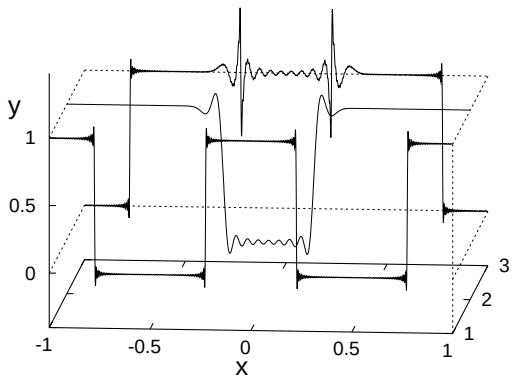

Figure 2.1: 1-dimensional unit impulse train expanded into Fourier$_{120}$ series, $\sum_{g=0}^{120} c_g^1 \cos\left(\frac{2\pi g x}{\Lambda}\right)$ (front). 1-d unit impulse function as a Hermite Gaussian$_{20}$ series, $\sum_{f=0}^{20} c_f^2 \psi_f^{w_d}(x)$ (middle). Inverted impulse train with centre impulse cancelled, $\sum_{f=0}^{20} c_f^2 \psi_f^{w_d}(x) - \sum_{g=0}^{120} c_g^1 \cos\left(\frac{2\pi g x}{\Lambda}\right)$ (back).// Notice the mismatch at the discontinuity between the series, limiting the gain of extending the Fourier series.

which may also be evaluated analytically. From these integrals we may now assemble the eigenvalue problem and solve for propagation constants and eigenvectors.

2.3.2 The Hermite Gaussian method

Expanding the cladding structure in a Fourier series does indeed make sense as long as the cladding structure is of a certain size. When the extent of the cladding structure diminishes, the assumptions implied may become invalid. To counteract this we suggest expressing the dielectric function as a superposition of a number of local expansion series. This allows us to scale the local expansions according to the size of the element being expanded, in analogy with the basic ideas behind wavelet theory. Thus, we may use relatively short expansion series, even if the the expanded features are small, and in this way retain efficiency in our calculations[10].

We expand the dielectric function in the following way[11]:

$$\epsilon(x,y) = \epsilon_{bg} + \sum_j (\epsilon_j - \epsilon_{bg}) \sum_{f,g}^{D} c_{f,g}^j \psi_{f,g}^{\omega_d^j}(x - r_x^j, y - r_y^j) \qquad (2.27)$$

where $c_{f,g}^j$ and ω_d^j denote expansion coefficients and the normalised characteristic width used for decomposition of the jth hole. ϵ_{bg} and ϵ_j are the dielectric constants of the background material and of the jth hole. D is the number of expansion terms used to decompose the holes[12]. The factors r_x^j and r_y^j denote the Cartesian coordinates of the position vector of the jth hole (fig 2.2). The characteristic width, ω_d, is not rigorously defined by any physical properties of the structure. In theory, as the Hermite Gaussian functions form a complete set regardless of characteristic width, it could be chosen arbitrarily. For simplicity we might set, $\omega_d \equiv 1$, which would indeed simplify the overlap integrals (eqs. 2.44...). In practise steps need to be taken to improve the convergence of the Hermite Gaussian series, if the efficiency gain of using localised functions is not to be lost. In the formulation (eq. 2.27) each defect is by scaled by its

[10] Since this method consists solely of Hermite Gaussian functions we name it the Hermite Gaussian method

[11] When holes overlap, this expression must be refined in order to be valid.

[12] In principle, this number could be chosen individually for each hole, but in the following we will, for simplicity, consider it to be equal for all holes.

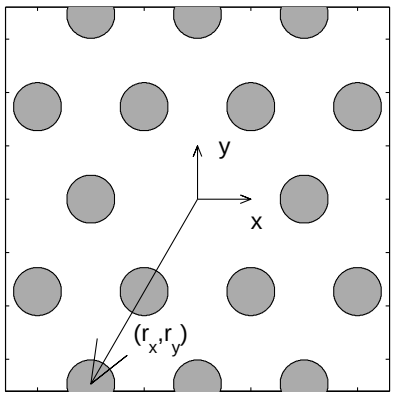

Figure 2.2: Schematic of a triangular lattice, small-core, PCF. $\boldsymbol{r}^j = (r_x^j, r_y^j)$ denotes the Cartesian coordinate vector of the jth hole.

dielectric constant, hence we may investigate expansion series behaviour by expansion of a unit height defect. Assuming defects to be circular we expand the function defined by:

$$f_{circ}(x,y) = u(1 - 4(x^2 + y^2)) \tag{2.28}$$

$$u(t) = \begin{cases} 0, & t < 0; \\ 1, & t \geq 0; \end{cases} \tag{2.29}$$

for a set of ω_d-values.
We see in figure 2.3 that the choice of characteristic width for the series has a tremendous impact on the convergence of the series. For accurate modelling it is, therefore, necessary to study the convergence behaviour of the expansion series as a function of the width parameter. We quantify the convergence of the series by numerically integrating the error (fig. 2.4):

$$\varepsilon = \iint_{\mathbb{R}^2} \left| f_{circ}(x,y) - \sum_{f,g} c_{f,g} \psi_{f,g}^{\omega_d}(x,y) \right| \mathrm{d}x\mathrm{d}y \tag{2.30}$$

Notice that the optimal choice of ω_d is dependent on the number of expansion functions. From figures 2.3 and 2.4 we conclude that a good general choice of characteristic width for circular defects is $\omega_d \approx 0.12$.

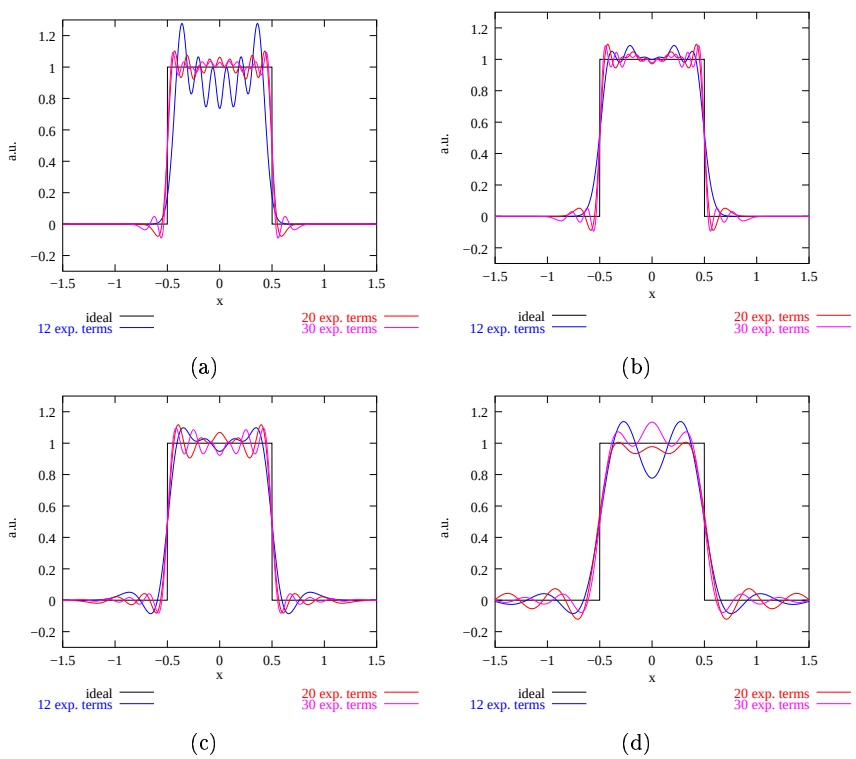

Figure 2.3: Slices along the x-axis of 2d circular, unit height, step function, $f_{circ}(x, y)$ (eq. 2.28), expanded into series of Hermite Gaussian functions for width parameters: (a) $\omega = 0.1$, (b) $\omega = 0.12$, (c) $\omega = 0.2$, (d) $\omega = 0.4$

.

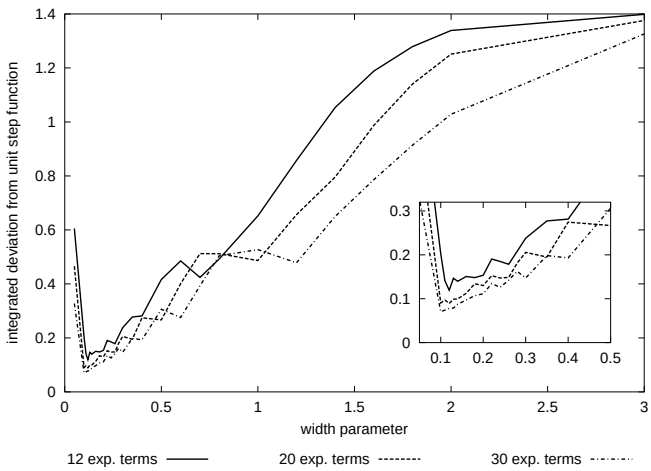

Figure 2.4: Integrated truncation error of Hermite Gaussian expansion-series from the circular unit step function, f_{circ} (eq. 2.28), where 12, 20 and 30 expansion terms have been used to expand the unit step.

Also notice that for certain values of ω_d, the truncation error temporarily rises as the number of expansion functions is increased. It is, therefore, of vital importance that ω_d is chosen carefully.

Determining the expansion coefficients of a particular shape generally involves performing an integral over the defect area. In the important case of a circular defect the overlap integral is analytically solvable — in other cases a numerical integration scheme has to be used. Due to the local nature of the defects, it may be more efficient to use numerical integration even in the case of a circular defect. Figure 2.5 shows the expansion coefficients along some rows in the expansion coefficient matrix (2.31) for $\omega_d = 0.12$.

$$C = C^T = \begin{pmatrix} c_{0,0} & \cdots & c_{0,D} \\ \vdots & \ddots & \vdots \\ c_{D,0} & \cdots & c_{D,D} \end{pmatrix} \tag{2.31}$$

Notice, that if ω_d may be held constant, due to the orthogonality of the expansion functions, we may "reuse" expansion coefficients when extending the expansion series, whereas they would have to be calculated anew, were the functions non-orthogonal.

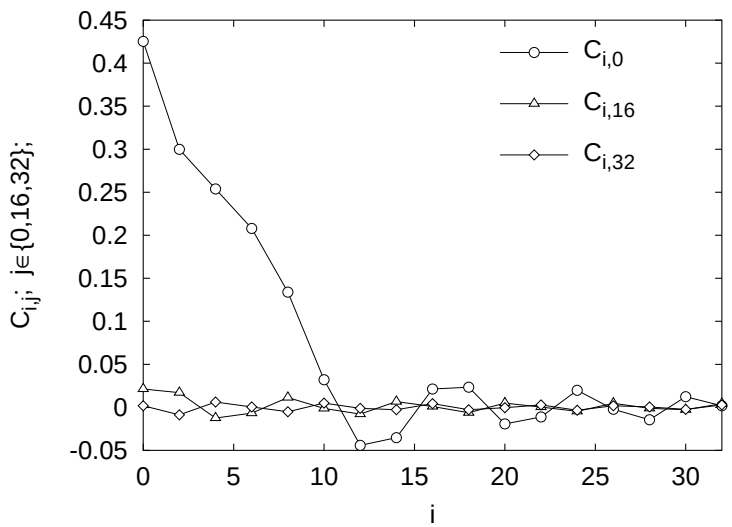

Figure 2.5: Expansion coefficients along three rows in the expansion matrix, for a circular defect expanded into an Hermite Gaussian series with $\omega_d = 0.12$.

For some applications, such as polarisation maintaining fibres, elliptical defects are highly interesting [19] [20]. Although it is, at present, unclear whether the practical problems in actually making such a fibre may be solved, it may theoretically represented within this framework by simply scaling the expansions through an anisotropic $\boldsymbol{\omega_d} \equiv (\omega_{d,x}, \omega_{d,y})$; $\omega_{d,x} \neq \omega_{d,y}$, and minor extensions to eqs. 2.14 through 2.18. Figure 2.6 shows expanded elements of different shapes, to indicate that any shape is indeed possible.
Square defects, for instance defined by (eqs. 2.28 & 2.29):

$$f_{square}(x,y)) = u(1-2|x|) \cdot u(1-2|y|) \tag{2.32}$$

appear even more difficult to control in a draw process (and, to the best of our knowledge, have yet to be shown in a PCF), conventional fibres with square (or indeed polygonal) claddings have been shown [21], suggesting that such defects might be achieved with improved drawing techniques. It is also plausible that square defects might be preferred over circular defects in an integrated optics context[13]. Upon inspection, the optimal choice of characteristic width for expanding a square defect, is $\omega_d = 0.12$, as for circular defects — this is not surprising since by definition (eqs. 2.28 & 2.32), the discontinuity of both types of defect, by definition, is at the same point on coordinate axes, i.e. for $|x|, |y| = 0.5$, although the volume of the square defect is larger.
To theoretically construct a triangular defect is also possible, but presents some practical difficulties. For instance, it is unclear as to where the origin of the expansion series should be chosen. The triangle's centre of gravity is a natural choice, but gives rise to poor convergence. A better choice is on one of the baselines of the triangle, but the series length necessary for an accurate description is still considerably longer than that of even defects, such as circles and squares.

Substituting eq. 2.27 into eqs 2.14 through 2.18 we may separate the

[13]Presently, the integrated photonic crystal community is concentrating on waves propagating in the plane, perpendicular to the defects, in which case squares are not advantageous over circles [22].

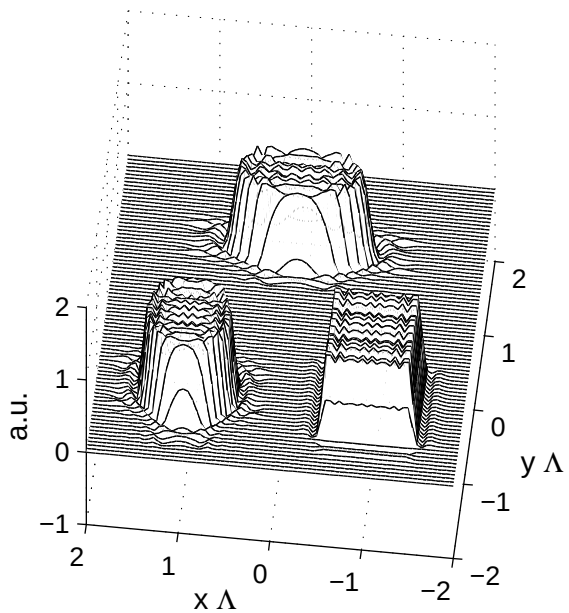

Figure 2.6: Three geometric elements of unit height, each expressed by a Hermite Gaussian expansion series of length 20.

two coordinates and write:

$$I^{(1)}_{abcd}(\omega_m) = I^{11}_{ac} I^{11}_{bd} \tag{2.33}$$

$$I^{(2)}_{abcd}(\omega_m) = \epsilon_{bg}\delta_{a,c}\delta_{b,d} + \sum_j (\epsilon_j - \epsilon_{bg}) \sum_{f,g}^{C} \gamma^j_{f,g} I^{22}_{acf} I^{22}_{bdg} \tag{2.34}$$

$$I^{(3)xx}_{abcd}(\omega_m) = \sum_j 2\left(\ln(\epsilon_{bg}) - \ln(\epsilon_j)\right) \sum_{f,g=0}^{C} \gamma^{(\ln),j}_{f,g} I^{22}_{acf} I^{31}_{bdg} \tag{2.35}$$

$$I^{(3)xy}_{abcd}(\omega_m) = \sum_j 2\left(\ln(\epsilon_{bg}) - \ln(\epsilon_j)\right) \sum_{f,g=0}^{C} \gamma^{(\ln),j}_{f,g} I^{35}_{acf} I^{34}_{bdg} \tag{2.36}$$

$$I^{(3)yy}_{abcd}(\omega_m) = \sum_j 2\left(\ln(\epsilon_{bg}) - \ln(\epsilon_j)\right) \sum_{f,g=0}^{C} \gamma^{(\ln),j}_{f,g} I^{31}_{acf} I^{22}_{bdg} \tag{2.37}$$

$$I^{(3)yx}_{abcd}(\omega_m) = \sum_j 2\left(\ln(\epsilon_{bg}) - \ln(\epsilon_j)\right) \sum_{f,g=0}^{C} \gamma^{(\ln),j}_{f,g} I^{34}_{acf} I^{35}_{bdg}, \tag{2.38}$$

$$I_{ac}^{11} = \int_{\mathbb{R}} \psi_a^{\omega_m}(x) \frac{\partial^2 \psi_c^{\omega_m}(x)}{\partial x^2} \mathrm{d}x \tag{2.39}$$

$$I_{acf}^{22} = \int_{\mathbb{R}} \psi_a^{\omega_m}(x) \psi_c^{\omega_m}(x) \psi_f^{\omega_d^j}(x - r_x^j) \mathrm{d}x \tag{2.40}$$

$$I_{acf}^{31} = \int_{\mathbb{R}} \frac{\partial \psi_a^{\omega_m}(x)}{\partial x} \psi_c^{\omega_m}(x) \frac{\partial \psi_f^{\omega_d^j}(x - r_x^j)}{\partial x} \mathrm{d}x \tag{2.41}$$

$$I_{acf}^{34} = \int_{\mathbb{R}} \psi_a^{\omega_m}(x) \psi_c^{\omega_m}(x) \frac{\partial \psi_f^{\omega_d^j}(x - r_x^j)}{\partial x} \mathrm{d}x \tag{2.42}$$

$$I_{acf}^{35} = \int_{\mathbb{R}} \frac{\partial \psi_a^{\omega_m}(x)}{\partial x} \psi_c^{\omega_m}(x) \psi_f^{\omega_d^j}(x - r_x^j) \mathrm{d}x \tag{2.43}$$

where $\gamma_{k,l}^j$ denotes the expansion coefficient of order k, l of the jth defect. Consequently, $\gamma_{k,l}^{(\ln),j)}$ is the k, l-order expansion coefficient of the logarithmic jth defect. Using the recursion formulae (eqs. 2.20 and 2.21), I^{31}, I^{34} and I^{35} may be expressed in terms of I^{22}. Thus, we need only solve integrals of the form:

$$\hat{I} = \int_{\mathbb{R}} \psi_a^{\omega_m}(x) \psi_c^{\omega_m}(x) \psi_f^{\omega_d^j}(x - r_x^j) \mathrm{d}x \tag{2.44}$$

to set up the eigenvalue problem. For $r_x = 0$ we may use use Feldheim's identity (eq. 2.45) [23] and odd-even function symmetry properties to reduce this integral to a summation. For $r_x \neq 0$, the integrand of eq. 2.44 is neither odd nor even. The integral may, however, be evaluated using the summation theorem for Hermite polynomials (eq. 2.46) [24]. It may be remarked that due to the local nature of the expansion functions, it may be efficient to use an adaptive numerical integration scheme considering the complexity of the solutions. This is particularly the case, when the order of the Hermite Gaussian functions is high, since the solutions involve Γ-functions on the same order as the polynomials, which makes them sensitive to numerical error.

$$H_a(x) H_b(x) = 2^b b! \sum_j^b \binom{a}{b-j} \frac{H_{a-b+2j}(x)}{2^j j!} \tag{2.45}$$

$$2^{\frac{a}{2}} H_a(x+y) = \sum_{j=0}^{a} \binom{a}{j} H_{a-j}\left(\sqrt{2}x\right) H_j\left(\sqrt{2}y\right) \tag{2.46}$$

2.4 Coupling coefficients and effective area

An orthonormal expansion of electromagnetic fields is practical for coupling considerations. In any physically deployed system containing optical fibres of any kind, which must, naturally, contain connections, it is important to consider coupling losses. Firstly, these losses arise from mismatch of mode-shapes [12], the magnitude of which may be closely approximated by eq. 2.47, where $\mathbf{H_1}$ $\mathbf{H_2}$ represent the magnetic fields of two modes coupling to each other. By orthonormality, the overlap integrals that need to be solved may be replaced by a summation over expansion coefficients of matching orders with no additional approximation needed.

$$\eta \approx \frac{\left[\iint_{\mathbb{R}^2} |\mathbf{H_1}(x,y) \cdot \mathbf{H_2^*}(x,y)|^2 \,\mathrm{d}x\mathrm{d}y\right]^2}{\left[\iint_{\mathbb{R}^2} |\mathbf{H_1}(x,y)|^2 \,\mathrm{d}x\mathrm{d}y\right]\left[\iint_{\mathbb{R}^2} |\mathbf{H_2^*}(x,y)|^2 \,\mathrm{d}x\mathrm{d}y\right]} \Rightarrow$$

$$\Rightarrow \eta \approx \frac{\left(\sum_{f,g=0}^{D} \mathcal{H}^x_{1,fg}\mathcal{H}^{x*}_{2,fg} + \mathcal{H}^y_{1,fg}\mathcal{H}^{y*}_{2,fg}\right)^2}{\left[\sum_{f,g=0}^{D}(\mathcal{H}^x_{1,fg})^2 + (\mathcal{H}^y_{1,fg})^2\right]\left[\sum_{f,g}(\mathcal{H}^{x*}_{2,fg})^2 + (\mathcal{H}^{y*}_{2,fg})^2\right]} \quad (2.47)$$

Thus, we may calculate coupling coefficients between modes in an a very efficient manner (see chapter 4).
Secondly, and often much more important, coupling losses arise from splice mismatch, i.e. when two fibre ends fail to line up correctly. We may define a coupling coefficient $\eta(r_x, r_y)$ where r_x and r_y denote the offset in Cartesian coordinates, and calculate the coupling coefficients through overlap integrals analogous to eq. 2.47. In this case we may, again take advantage of the summation theorem for Hermite polynomials (eq. 2.46) to express the coupling coefficients[14]. It is of course also of interest to consider coupling between a conventional step index fibre and a PCF. To a good approximation level we may represent the field of the fundamental mode in a step index fibre as a Gaussian, $|F_2(x,y)| = e^{-\frac{x^2+y^2}{2\sigma^2}}$ [12]. In

[14] Clever reuse of the integrals evaluated in equation 2.44 may expedite these calculations

this case the coupling coefficient may be expressed as:

$$\eta \approx \frac{\left[\sum_{f,g=0}^{D} \mathcal{H}_{fg}^{x} \left(\int_{\mathbb{R}} e^{-\frac{x^2}{2\sigma^2}} \psi_f^{\omega_m}(x)\mathrm{d}x\right)\left(\int_{\mathbb{R}} e^{-\frac{y^2}{2\sigma^2}} \psi_g^{\omega_m}(y)\mathrm{d}y\right)\right]^2}{\left[\sum_{f,g=0}^{D} (\mathcal{H}_{1,fg}^{x})^2 + (\mathcal{H}_{1,fg}^{y})^2\right]\left[2\pi\sigma^2\right]} \tag{2.48}$$

The integrals in the numerator of eq. 2.48 are analytically solvable [16]:

$$\int_{\mathbb{R}} e^{-\frac{x^2}{2\sigma^2}} \psi_f^{\omega_m}(x)\mathrm{d}x = (-1)^{\frac{f}{2}} \pi^{\frac{1}{4}} \omega_m^{\frac{1}{2}} 2^{-\frac{f}{2}} \frac{(f!)^{\frac{1}{2}}}{\left(\frac{f}{2}\right)!} \frac{a^f}{(1+a^2)^{\frac{f+1}{2}}} \tag{2.49}$$

$$a^2 = \left(\frac{1}{2} + \frac{\omega_m^2}{2\sigma^2}\right); \quad f \text{ even}$$

In many situations the effective area of a mode is an important parameter. This is especially the case when non-linear effects, such as Raman and Brioullin scattering, are to be considered [25] [26] [27]. Given the high effective index contrast possible in PCFs, the intensity in a fibre may be very high, increasing non-linear effects. We may express the effective area as [28]:

$$A_{eff} = \frac{\left(\iint_{\mathbb{R}^2} |\boldsymbol{F}(x,y)|^2 \,\mathrm{d}x\mathrm{d}y\right)^2}{\iint_{\mathbb{R}^2} |\boldsymbol{F}(x,y)|^4 \,\mathrm{d}x\mathrm{d}y} \tag{2.50}$$

Again, orthogonality is instrument in efficient calculations of the resulting overlap integrals, although the denominator of eq. 2.50 becomes rather complicated [15].

2.5 Summary of chapter 2

In this chapter we have established the theoretical framework of the proposed purely Hermite Gaussian function series based modelling procedure. Firstly, we have discussed the general steps of overlap integrals transforming Maxwell's equations for propagating waves[15] into a matrix eigenvalue problem by performing overlap integrals. Thereafter we have briefly discussed the possible descriptions of the dielectric function of the structure under study, that constitute the Localised Function Methods known in the

[15] In the scalar case: Helmholtz' equation.

literature. This lead into a detailed discussion of our proposed expansion scheme expressing the dielectric as a sum of parts.

Once the eigenvalue problem has been assembled, it may be solved using standard eigenvalue solvers, where the eigenvalues and eigenvectors directly represent the modal index (or propagation constant), and electromagnetic field distribution, respectively, in the sense that the eigenvectors consist of expansion series coefficients of the fields.

We have also discussed expressions for key features such as coupling to and from fields described by Hermite Gaussian series, as well as the nonlinear effective area.

References to chapter 2

[1] A. Graps. "An introduction to wavelets", *IEEE Computational Science and Engineering*, vol. 2, no. 2, pp. 50–61, 1995.

[2] T. M. Koornwinder, editor. *Wavelets: An elementary treatment of theory and applications*. World Scientific, 1993.

[3] J. P. Albert, C. Jouanin, D. Cassagne, and D. Bertho. "Generalized wannier function method for photonic crystals", *Physical Review B*, vol. 61, no. 7, pp. 4381–4384, 2000.

[4] D. Mogilevtsev, T. A. Birks, and P. S. Russel. "Group velocity dispersion in photonic crystal fibers", *Optics Letters*, vol. 23, no. 21, pp. 1662–1664, 1998.

[5] T. M. Monro, D. J. Richardson, N. G. R. Broderick, and P. J. Bennett. "Holey optical fibers. an efficient modal model", *Journal of Lightwave Technology*, vol. 17, no. 11, pp. 2078–2081, 1999.

[6] M. Bayindir, E. Cubukcu, I. Bulu, and E. Ozbay. "Photonic band-gap effect, localization, and waveguiding in the two-dimensional penrose lattice", *Physical Review B*, vol. 63, no. 16, pp. 161104–1–161104–4, 2001.

[7] T. M. Monro, P. J. Bennett, N. G. R. Broderick, and D. A. Richardson. "Holey fibers with random cladding distributions", *Optics Letters*, vol. 25, no. 4, pp. 206–208, 2000.

[8] J. D. Joannopoulos, R. D. Meade, and J. N. Winn. *Molding the flow of light*. Princeton University Press, 1995.

[9] R. D. Meade, A. M. Rappe, K. D. Brommer, J. D. Joannopoulos, and O. L. Alerhand. "Accurate theoretical analysis of photonic band-gap materials", *Physical Review B*, vol. 48, no. 11, pp. 8434–8437, 1993.

[10] S. G. Johnson and J. D. Joannopoulos. "Block-iterative frequency domain methods for maxwell's equations in a planewave basis", *Optics Express*, vol. 8, no. 3, pp. 173–190, 2001.

[11] J. P. Albert, C. Jouanin, D. Cassagne, and D. Monge. "Photonic crystal modelling using a tight-binding wannier function method", *Optical and Quantum Electronics*, vol. 34, no. 1-3, pp. 251–263, 2002.

[12] A. W. Snyder and J. D. Love. *Optical waveguide theory*. Kluwer Academic Publishers, 2000.

[13] T. P. White, R. C. McPhedran, C. M. de Sterke, L. J. Botten, and M. J. Steel. "Confinement losses in microstructured optical fibers", *Optics Letters*, vol. 26, no. 21, pp. 1660–1662, 2001.

[14] D. Mogilevtsev, T. A. Birks, and P. S. Russel. "Localized function method for modeling defect modes in 2-d photonic crystals", *Journal of Lightwave Technology*, vol. 17, no. 11, pp. 2078–2081, 1999.

[15] T. M. Monro, D. J. Richardson, N. G. R. Broderick, and P. J. Bennett. "Modelling large air fraction holey optical fibers", *Journal of Lightwave Technology*, vol. 18, no. 1, pp. 50–56, 2000.

[16] N. N. Lebedev. *Special functions and their applications*. Dover Publications, 1972.

[17] F. S. Acton. *Numerical methods that work*. Harper & Row, 1970.

[18] K. Okanoda. *Optical properties of photonic crystals*. Springer Verlag, 2001.

[19] M. J. Steel and R. M. Osgood. "Elliptical-hole photonic crystal fibers", *Optics Letters*, vol. 26, no. 4, pp. 229–231, 2001.

[20] M. J. Steel and R. M. Osgood. "Polarization and dispersive properties of elliptical-hole photonic crystal fibers", *Journal of Lightwave Technology*, vol. 19, no. 4, pp. 495–503, 2001.

[21] K. Yoshida and T. Morikawa. "Optical fibers with polygonal cladding", *Optical Fiber Technology*, vol. 3, no. 3, pp. 273–277, 1997.

[22] T. F. Krauss and R. M. de la Rue. "Photonic crystals in the optical regime — past present and future", *Progress in Quantum Electronics*, vol. 23, no. 2, pp. 51–96, 1999.

[23] E. Feldheim. "Qulques nouvelles relations pour le polynomes dhermite", *Journal of the London Mathematical Society*, vol. 13, pp. 22–29, 1938.

[24] I. M. Gradshteyn and I. M. Ryzhik, editors. *Table of integrals, series and products*. Academic Press, Fourth edition, 1980.

[25] R. H. Stolen and E. P. Ippen. "Raman oscillation in glass optical waveguide", *Applied Physics Letters*, vol. 20, no. 2, pp. 62–64, 1972.

[26] E. P. Ippen and R. H. Stolen. "Stimulated brioullin scattering in optical fibers", *Applied Physics Letters*, vol. 21, no. 11, pp. 539–541, 1972.

[27] R. H. Stolen. "Relation between the effective area of a single-mode optical fiber and the capture fraction of spontanetous raman scattering", *Journal of the Optical Society of America B*, vol. 19, no. 3, pp. 498–501, 2002.

[28] G. P. Agrawal. *Nonlinear fiber optics*. Academic Press, Third edition, 2001.

Chapter 3

Hermite Gaussian simulations

In this chapter we proceed to use the model described in the preceding chapter, to simulate a range of different structures. We start out with a much studied fibre structure, namely the triangular, small core, index guiding fibre, to verify the model and its limitations, proceeding with a variation on the simplest triangular lattice fibre that may be more suitable for applications (sec. 3.1). Thereafter we examine a quadratic lattice fibre (sec. 3.2), and a novel, pentagonal symmetric fibre design (sec. 3.3) in order to showcase the flexibility of the modelling procedure. In section 3.4 we further examine limitations and possibilities of the model by testing it on a honeycomb photonic bandgap fibre. We end this chapter with simulations of variations of the so called "onion"-fibre (sec. 3.5), where air holes are used to effectively form high contrast, concentric circles around a core region [1].

As noted in the introduction, manufacturing tolerances for index guiding PCFs are, by nature, less stringent than for their photonic bandgap counterparts. This has lead to a concentration of research on index guiding fibres in the early years of PCF studies. As the localised functions methods force localised solutions there is an inherent problem in modelling bandgap structures, since the bandgaps are formed by interactions between many lattice periods in a crystal. Also, keeping in mind that cladding modes are not resolved well, for index guiding fibres, simple external means of determining whether modes are guided or not, exist [2] [3]. Finding the fundamental guided mode of the fibre becomes a simple a matter of sorting the eigenvalues of eq. 2.9 by magnitude. The effective index approach, or plane-wave method on a single-cell lattice, may be used to determine cutoff-wavelengths for higher order modes.

As mentioned above we have chosen to implement this method with expansion series along the Cartesian axes. This implies a favouring of structures with a four-fold rotational symmetry.

3.1 Triangular lattice, index guiding structures

Our first case study is the triangular lattice, index guiding fibre. This has been extensively studied, in the literature, theoretically as well as experimentally. It therefore serves well as a test case for the model. An issue with all functions approximated using Hermite Gaussian expansion series, as defined in equations 2.5 and 2.6, is the inclusion of the series character-

istic width. As discussed it has a major impact on the convergence of the function series when expanding the dielectric function. This, of course, applies to the electromagnetic fields, found as solutions to the eigenvalue problem, as well. It is, therefore, necessary to validate the choice of characteristic width for each type of structure, as the optimal choice may (in fact is expected to), vary depending on the fibre geometry.

3.1.1 Small-core triangular fibre

This fibre is one the most studied so far and so is a reasonable choice as a validation measure for the model. One of the reasons that this structure has been so extensively studied is that it is relatively simple to make, by simply stacking glass tubes on top of each other. The holes will then form a triangular lattice. By replacing one tube with a solid glass rod, a core is formed. The tubes may then be fused together and drawn using conventional fibre drawing techniques[1] Unless the tubes have a hexagonal circumference, interstitial holes remain between the tubes after stacking. Because of their comparatively small diameter, however, they tend to collapse during draw and only contribute negligibly to the properties of the fibre. Figure 3.1 shows a SEM- (Scanning Electron Microscope) picture of a simple triangular structure. Notice the absence of interstitial holes.

It is common in the photonic crystal fibre community to let the scale of the structures be defined by two parameters, namely the lattice pitch and the hole diameter, commonly denoted Λ and d[2] (fig. 3.2). The pitch defines the overall size of the lattice, to which all other measures are commonly normalised. This allows for scaling of results to any desired wavelength, if material effects are neglected. Although Ferrando et. al. have suggested another pair of parameters more suitable for dispersion-tailoring of fibres of this type [4], we shall adhere to this practise.

The discussion on scaling the expansion series according to the features of the underlying function (chapter 2) also applies to the electromagnetic

[1] In practise, this is true to some extent only. In order to achieve low losses, care has to be taken to prevent polluting elements from entering the glass during the stacking process. (Preferably this should be down in a clean-room, which vastly increases the manufacturing costs.). In comparison, a conventional fibre preform may easily be made in a closed environment process, such as CVD (Chemical Vapour Deposition).

[2] The 2nd parameter is naturally only meaningful when all the holes are of equal size

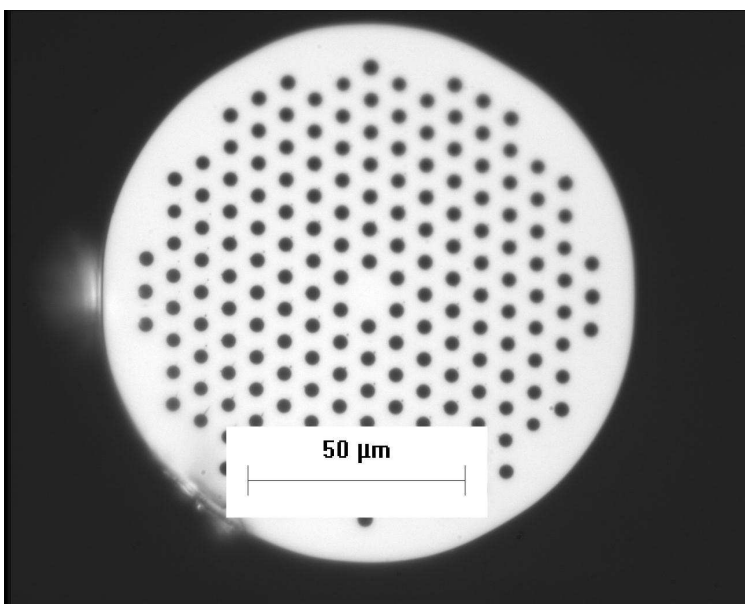

Figure 3.1: End face of an endlessly single mode, triangular Photonic Crystal Fibre. Notice that no interstitial holes remain. *Courtesy of Crystal Fibre A/S*

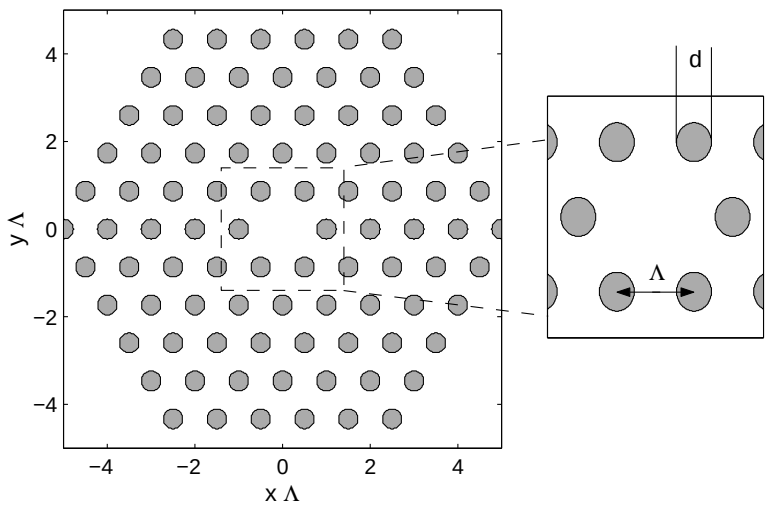

Figure 3.2: Schematic drawing of a 5-ring triangular PCF. The closeup show two important parameters: The lattice spacing, or pitch, Λ, and the hole diameter, d, which are commonly used to describe the scale of a structure.

field solutions, with the important difference that an absolute measure of convergence no longer exists. It is conceivable to choose the best possible fit with another modelling scheme such as the plane wave method. This would, however, make this procedure equally dependent on an infinite cladding structure. Instead we proceed by performing the overlap integrals as outlined previously (sec. 2.3.2) and solve the associated eigenvalue problem for several different values of ω_m at different wavelengths – to find an interval, where the modal indices depend weakly on the characteristic width, i.e. where the convergence of the series is reasonably fast (fig. 3.3). Differentiating β/k with respect to ω_m yields two overall inflection points[3], $\omega_m \approx 0.6$ and $\omega_m \approx 0.85$, around which the eigensolutions may be considered stable to second order. Keeping in mind that the expansion series behaviour for the dielectric function showed several local minima (fig 2.4), it is not surprising to find more than one candidate for ω_m. We may also recall that although the optimal characteristic width does indeed vary with expansion series length, D, we may find an average choice that is reasonable for a range of Ds. By varying D in the whole ω_m-range we identify an overall stability region around $\omega \approx 0.6$. We may note that this is in agreement with what has been used by Monro et al. [5]. This is in agreement with effective index analysis found in the literature [6], where it is argued that the equivalent step index fibre should have a core radius of 0.625Λ, as the optimal characteristic width should reflect the width of the underlying function[4].

The remaining parameter to evaluate is the number of basis functions needed for stable solutions to the eigenvalue equation(eq. 2.9). Choosing $\omega_m = 0.6$ in the stable region, we consider solutions as a function of normalised frequency, Λ/λ, for some different numbers of basis functions (figs. 3.1.1 and 3.1.1). From this we draw the conclusion that in the higher frequency-range the eigenvalues are sufficiently converged for 20 and 12 basis functions in the structure and field expansions, respectively. As the frequency decreases, however, we also see that an increase in expansion functions reveals a "return" towards the core index. This implies that the fields now spread so far into the cladding that the effect of the surrounding glass becomes non-negligible, and that a longer, $D > 12$, expansion series

[3]The exact positions depend on the wavelength.

[4]The optimal ω_m is larger than the corresponding ω_d, due to the less sharp nature of the field functions.

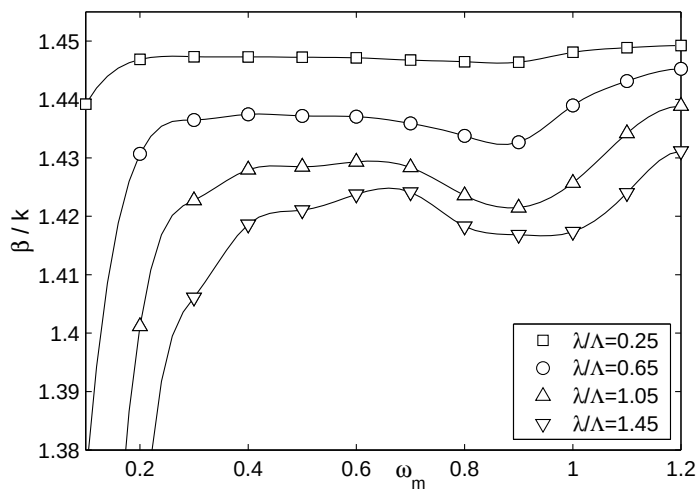

Figure 3.3: Modal index, β/k, for the fundamental mode vs. characteristic width, ω_m, as calculated at four wavelengths with Hermite Gaussian functions, with 20 and 12 expansion functions for the holes and the fields, respectively. The structure considered is a 5-ring triangular PCF with $d/\Lambda = 0.30$.

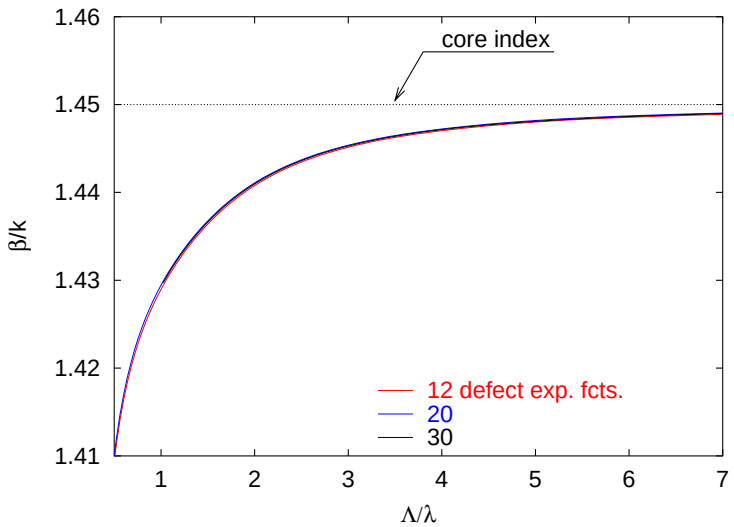

Figure 3.4: Modal indices, β/k, vs. normalised frequency, Λ/λ, for three defect expansion series of different lengths, for a 5-ring triangular, close packed structure, with $d/\Lambda = 0.30$ and 12 terms in the field-expansion series. Notice that the curve showing the expansion with 20 defect-expansion functions coincides almost completely with the curve for 30 functions.

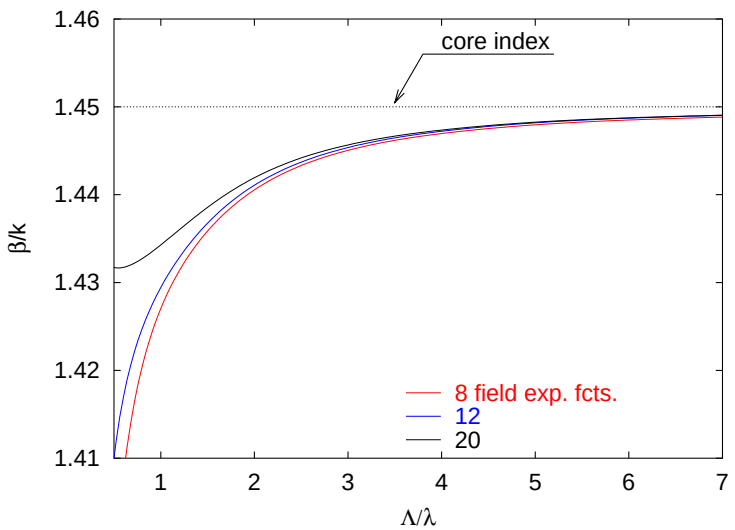

Figure 3.5: Modal indices, β/k, vs. normalised frequency, Λ/λ, for three field-expansion series of different lengths, for a 5-ring triangular, close packed structure, with $d/\Lambda = 0.30$ and 20 expansion terms in the defect expansion series.

is needed to express the solutions accurately.

We proceed by solving the wave equations for several different hole-sizes to evaluate their effect on the solutions. The highest two resulting eigenvalues, representing modal indices of the fundamental mode and its counterpart, polarised in the other principle direction, are shown in fig.3.6.

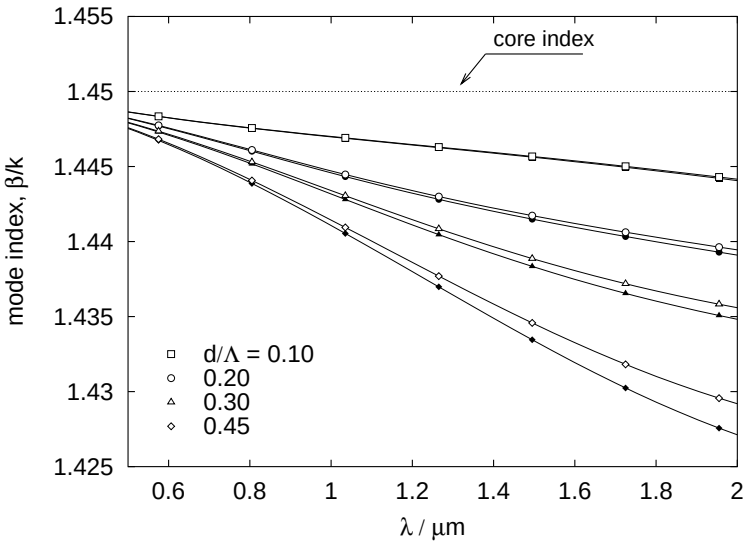

Figure 3.6: Modal indices of the fundamental guided mode for a 5-ring, close-packed, triangular PCF with $d/\Lambda = 0.10 \ldots 0.45$, calculated with 20 expansion functions, a pitch: $\Lambda = 2.3\mu m$ and a characteristic width of: $\omega = 0.5$. The open symbols denote predominantly y-polarised solutions, closed symbols x-dominant solutions.

Given the solutions of the eigenvalue problem, we may readily calculate the magnetic field distribution in the modelled structure, from the associated eigenvectors of eq. 2.9. Fig. 3.7 shows the transverse component of the magnetic field distribution for two different hole-sizes. Notice the hexagonal shape of the mode, which agrees with the symmetry of the structure and previous calculations of triangular structures [2] [7] [5].

Clearly, there is a dominant direction of the mode. Thus, the symmetry arguments of Steel et. al. [8] are applicable, stating that a PCF

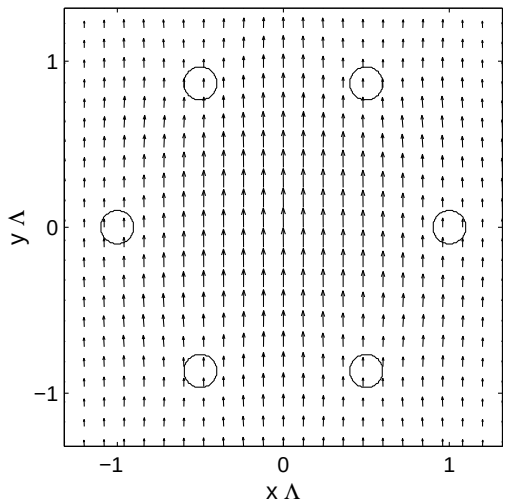

(a)

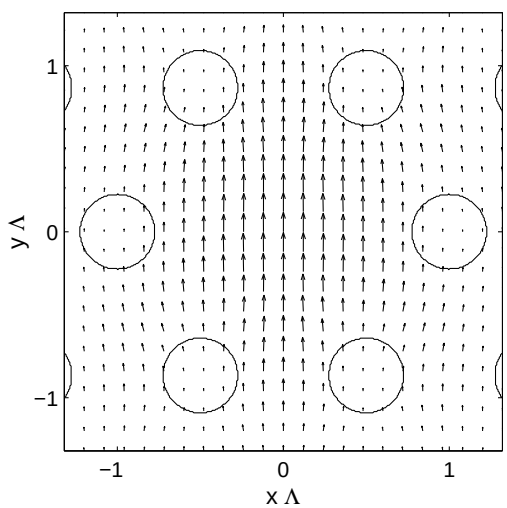

(b)

Figure 3.7: Transverse magnetic field vectors for the fundamental mode of a 5-ring, close-packed, triangular PCF, with $\Lambda = 1.0\mu m$ at $\lambda = 850nm$ and hole diameter, d/Λ = (a) 0.20, (b) 0.45, using 20 field expansion functions

with m-fold rotational symmetry, $m > 2$, cannot be birefringent. Hence, we may consider the fibre as being non-birefringent. If we again view the modal indices as a function of wavelength (fig. 3.6), the second eigensolution should, by symmetry, be exactly degenerate with the first. Clearly, this is not the case, indicating an error in the eigenvalues. This is an effect arising from the Cartesian expansion axes used which do not reflect the symmetry of the structure (cf. sec. 3.2). This could be counteracted by simply using a longer expansion series, or by by using another set of expansion axes, which would imply reformulating the overlap integrals (eqs. 2.14 and 2.18) to include cross terms between coordinates. If we now view the intensity profile, shown in fig. 3.10, of the fundamental mode in the triangular small core fibre we see more clearly that it matches the symmetry of fibre geometry. We also note that, as expected [7], a longer wavelength tends to push the fields further into the air-holes.

In conventional fibre technology the mode field diameter [9] of the fundamental mode, is often used to quantise the extent of the mode. A large mode-field diameter is often wanted, since it renders the fibre less sensitive to splice mismatch, making coupling into the fibre less complicated. For a PCF, with its inherently non-circular mode shape, the mode field diameter loses its meaning and may only be replaced by an average mode field diameter. We study this by viewing the radius where the intensity of the modal field has dropped to e^{-2} of its centre (maximal) value, as a function of wavelength and hole diameter (fig. 3.8) in the two principal directions of the fibre. The e^{-2}-radius rises with wavelength and is greater in the y-direction as expected. If the holes become small, however, we note that the radius tends to toward a finite value, implying that the basis functions are no longer able to resolve the fields properly, i.e. that a longer expansion series is needed. This effectively limits the parameter space where the method is useful, since the expansion series length itself is limited by numerical errors in the overlap integral calculations and by the size of the eigenvalue problem, in the sense that the calculation time gain of localisation is lost. We now define an optimal Gaussian coupling coefficient, η_{tri}, as the coupling efficiency between a guided mode and a Gaussian field scaled to maximise coupling (eq. 2.47), to get a scalar measure of coupling to the fibre. We find that coupling efficiency drops significantly as the wavelength increases and as the hole-size is reduced (fig. 3.9).

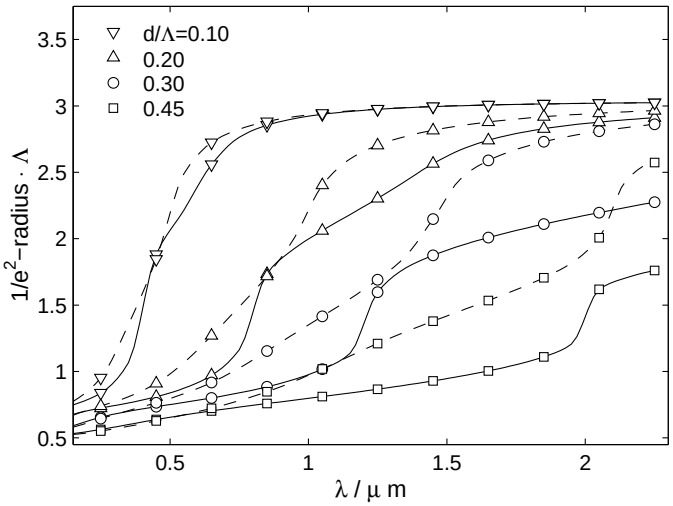

Figure 3.8: e^{-2}-radius as a function of wavelength for the fundamental mode of 5-ring, triangular PCF with $d/\Lambda = 0.10 \ldots 0.45$ for the principal directions x=solid, and y=dashed.

As stressed before, one of the main strengths of the localised function methods lies in the orthogonality of the expansion functions. In the same way we took advantage of the orthogonality when formulating the eigenvalue problem 2.9, we may easily integrate fields over the infinite transverse plane, by replacing the integrals with a sum of the field expansion coefficients, for instance enabling efficient coupling coefficient calculations between fields (eq. 2.47 and chapter 4) or evaluation of the mode effective area [10] (eq. 2.50).

Another important difference between conventional fibres and PCFs, is their dispersion characteristics. PCFs consisting of a silica-air system with a high index core, will always fundamentally display the material dispersion characteristics of silica on a large wavelength scale, yet on account of the highly wavelength dependent behaviour of the cladding it is possible to target dispersion characteristics impossible in conventional fibre technology [4]. Assuming non-linear effects to be negligible we may readily calculate the dispersion in the PCF, once we have solved the eigenvalue problem, from the obtained eigenvalues [11] [12] (fig. 3.12). These dispersion characteristics are in reasonable agreement with results reported

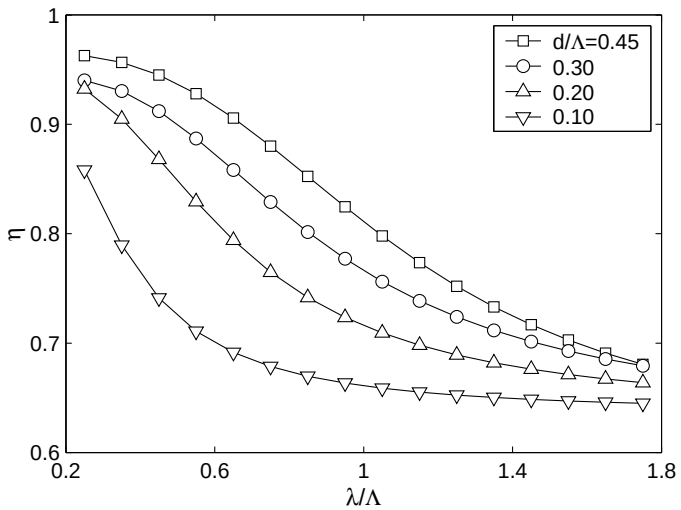

Figure 3.9: Optimal Gaussian coupling efficiency toward a triangular small core PCF, with $d/\Lambda = 0.10 \ldots 0.45$.

with the localised function method [5] and experimentally [13], albeit the latter was measured in a rather deformed fibre.

3.1.2 Large-core triangular fibre

Although PCFs may in theory be scaled to fit any wavelength, in practise the structure size must be on the same order as the wavelength, in order to avoid such unwanted effects, as bending loss [6] [14]. Hence the core diameter of the simple triangular structure is of the same order as the wavelength. For many applications this is impractical as it puts very strict tolerances on connectors and splices. One way of ameliorating this problem is to replace several of the inner glass cylinders with solid rods in the stacking process, thereby creating a larger core[5].

We investigate this further by removing the innermost ring of holes in the simple triangular structure, creating a fibre with a core radius, $a \approx 2\Lambda$. The other rings are left in place (fig. 3.13).

[5]The presence of many interfaces between stacking elements in the core, where the intensity is at its highest, has been shown not to significantly influence the overall loss of the fibre [15].

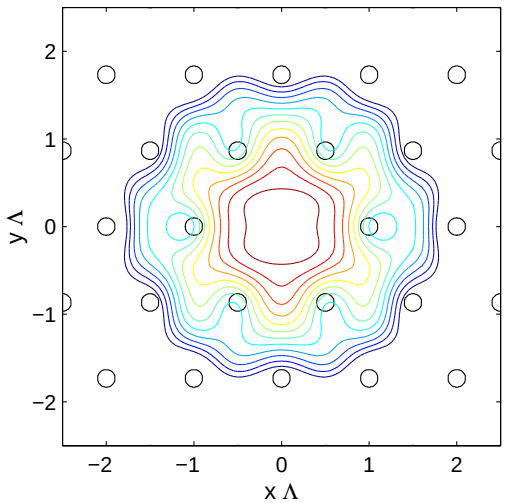

(a)

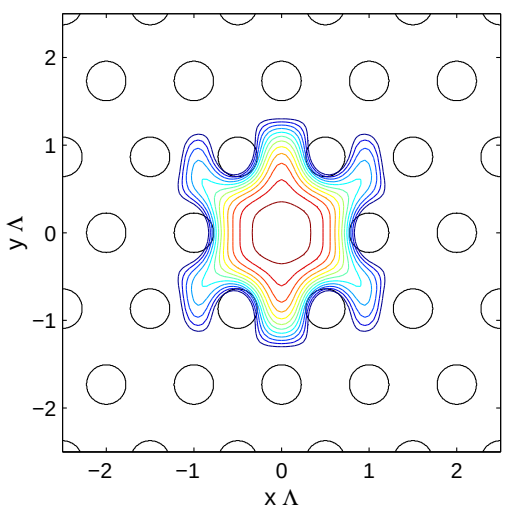

(b)

Figure 3.10: Squared magnetic field distribution of small core, triangular lattice, 5-ring PCF, with (a): $d/\Lambda = 0.20$ and (b) $d/\Lambda = 0.45$, at $\lambda/\Lambda = 0.85$. Contours are spaced $2dB$ apart between $-2dB$ and $-24dB$.

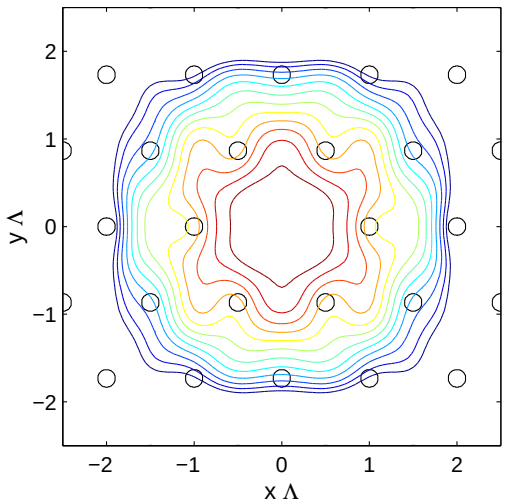

(a)

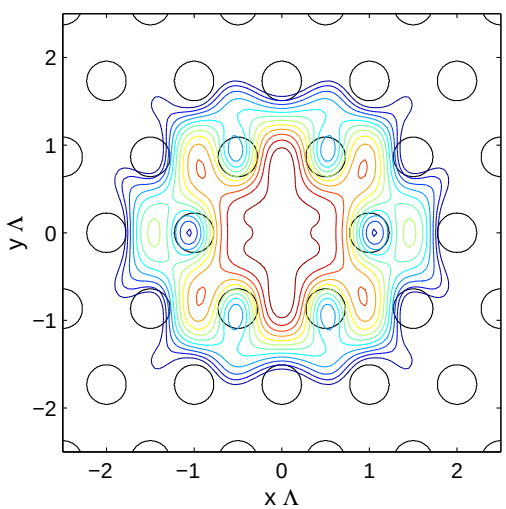

(b)

Figure 3.11: Squared magnetic field distribution of small core, triangular lattice, 5-ring PCF, with (a): $d/\Lambda = 0.20$ and (b) $d/\Lambda = 0.45$, at $\lambda/\Lambda = 1.55$. Contours are spaced $2dB$ apart between $-2dB$ and $-24dB$.

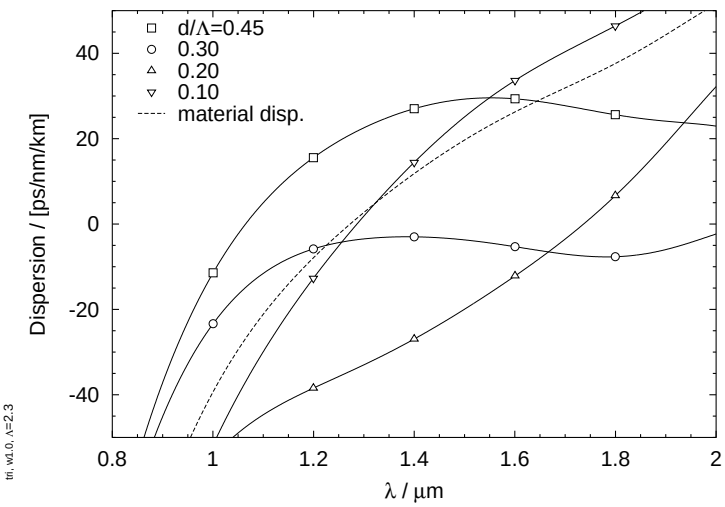

Figure 3.12: Dispersion characteristics of triangular, small core fibres, with 5 rings of holes, for $d/\Lambda = 0.10 \ldots 0.45$ and lattice pitch, $\Lambda = 2.3\mu m$, material dispersion of silica included.

Due to the increased core size of this fibre, the eigenvalue solutions, obtained through eq. 2.9, are expected to exhibit a different ω_m-dependence. Again (sec. 3.1.1), we calculate the eigenvalues for several different characteristic widths, in order to locate a region which has stable solutions for a small number of expansion functions. Clearly the power distribution spreads (fig. 3.14), as expected, more than in the small core case. Further analysis of the fundamental mode for fibres of this type shows a gain in mode effective area between > 3 for $d/\Lambda = 0.45$, at $\lambda/\Lambda = 0.25$ to a gain of approximately unity for $d/\Lambda = 0.10$ (fig. 3.19). In the small hole case, however, one must remember that we are close to the localisation limit of the model. Hence, there is significant uncertainty in the effective area measure in this case.

3.2 Quadratic lattice index guiding fibre

Most of the PCFs considered in the literature so far have been variations on the triangular lattice, whereas the properties of photonic crystals

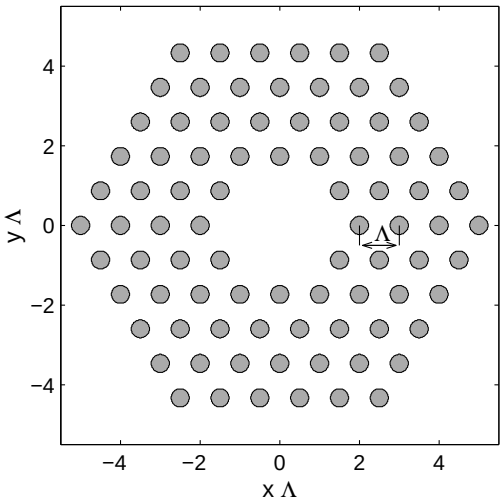

Figure 3.13: Schematic drawing of a large core, triangular lattice, PCF with $d/\Lambda = 0.30$.

with a quadratic lattice have been more extensively studied in planar, integrated photonic crystal waveguides. As discussed earlier, the main reason for the concentration on triangular lattice structures, is the relative ease with which one may manufacture a fibre-preform by a, in theory, simple stacking procedure using circular elements. A quadratic lattice may also be stacked using circular cylinders and rods. It would, however, be necessary to include another element (for instance circular rods with $d_0 = (\sqrt{2} - 1)\Lambda$), for the stack to be stable (fig. 3.15).

We briefly investigate the properties of a quadratic lattice, small core PCF, using the Hermite Gaussian model. In this case the principal symmetry axes of the structure coincide with the Cartesian coordinate axes, which is beneficial to the convergence of the expansion series. We follow the procedure established above for modelling a new type of fibre, and solve the eigenvalue problem for a number of characteristic widths. The core volume in this fibre is larger than that of the corresponding triangular fibre (sec. 3.1.1), and that the air filling fraction [7] is correspondingly lower. We note from section 2.3.2, page 28, that even though its volume is larger, the characteristic width of the quadratic defect expansions has an optimum at approximately the same value as the circular defect ex-

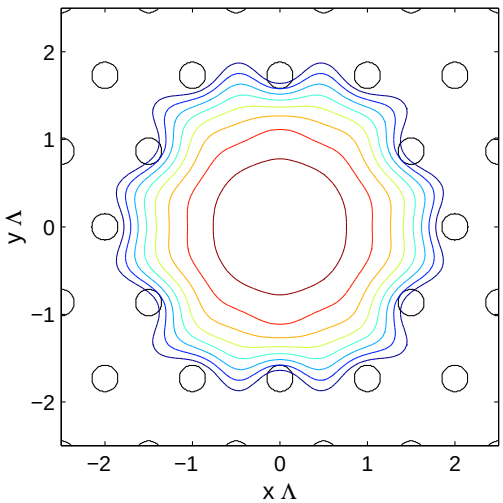

Figure 3.14: Squared magnetic field distribution of large core, triangular lattice, 5-ring PCF, with $d/\Lambda = 0.45$, at $\lambda/\Lambda = 0.85$. Contours are spaced $2dB$ apart between $-2dB$ and $-24dB$.

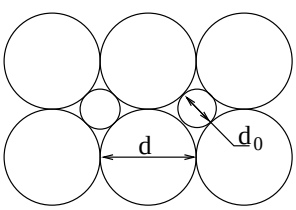

Figure 3.15: Stacking diagram of a quadratic lattice PCF.

pansion. Therefore we expect the optimal ω_m to not differ much from the triangular optimum. A specific study of ω_m along the lines outlined in section 3.1 shows first order zeros at $\omega_m \approx 0.6$ and $\omega_m \approx 1.0$. Further study of the field distributions shows that a good choice in this case is $\omega_m = 0.6$. Fig. 3.17 shows a field distribution of the fundamental mode in this fibre at a wavelength in the middle of the interval for two hole sizes.

Since the symmetry of the fibre coincides with the expansion axes, the erroneous numerical birefringence seen in the triangular fibre is not present to the same extent when modelling this fibre. No evidence of the erroneous numerical birefringence seen in the triangular fibres 3.1 is found

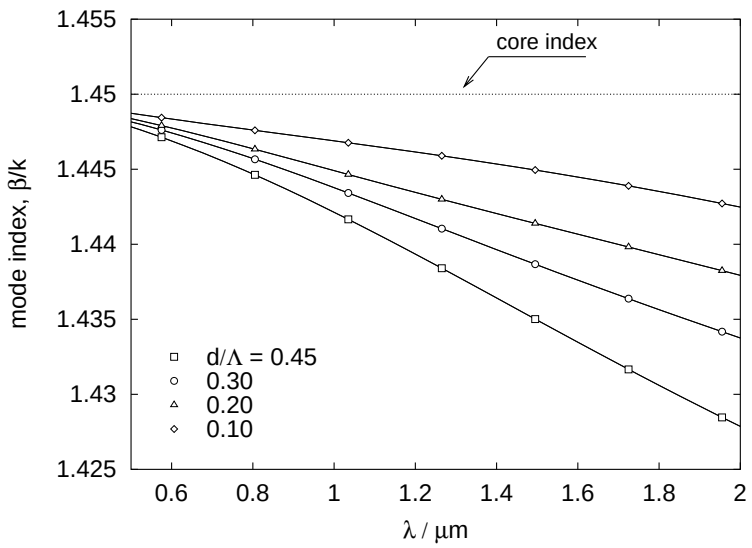

Figure 3.16: Modal indices of the fundamental guided mode for a 5-ring, quadratic lattice PCF with $d/\Lambda = 0.10 \ldots 0.45$, calculated with 12 expansion functions, a pitch: $\Lambda = 2.3\mu m$ and a characteristic width of: $\omega = 0.6$. The open symbols denote predominantly y-polarised solutions. The x-dominant solution (solid symbols) is completely covered as the mode is degenerate (to machine precision).

in the quadratic lattice fibre (fig. 3.16). In fact for the whole frequency interval studied the numerical birefringence of the quadratic lattice fibre is on the order of machine precision, when using as little as 12 expansion functions. This is because the symmetry of the fibre coincides with the expansion axes.

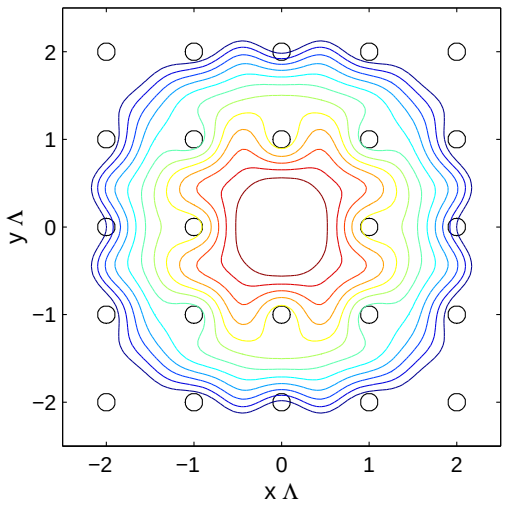

(a)

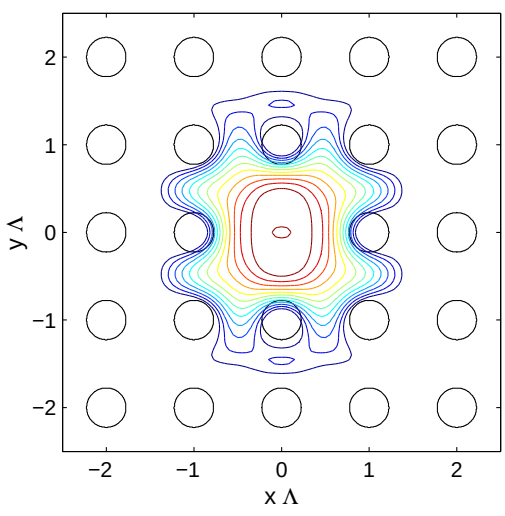

(b)

Figure 3.17: Squared magnetic field distribution of quadratic lattice 5-ring PCF, with (a) $d/\Lambda = 0.20$ and (b), at $\lambda/\Lambda = 1.05$. Contours are spaced $2dB$ apart between $-2dB$ and $-24dB$.

3.3 Pentagonal structure

So far we have only considered lattice structures that may be fabricated by the simple stack and draw technique. A strong point of the model used, is that there is no formal restriction on the kinds of structures that may be considered other than that of a localised mode. In the high index case there is always a fundamental mode bound to the core. Thus, any kind of structure with an effective cladding index lower than that of the core may be considered. Monro et.al. [16] have shown that even a fibre structure with holes randomly distributed in the cladding may guide light, as long as the holes are spread fairly evenly in the cladding. To stress this versatility of the modelling procedure, we construct a pentagonal fibre, where the hole positions are given by

$$\boldsymbol{r}_{j,k} = \Lambda j\hat{\boldsymbol{r}} + \frac{2\pi}{5j}k\hat{\boldsymbol{\theta}} \tag{3.1}$$
$$k \in 0\ldots 5; \quad j \in 1..\#rings$$

This kind of fibre may presently not be of much practical interest, since it is a challenging task to fabricate it using common "stack-and-draw" techniques. At present, a more feasible technique, currently developing for material systems other than silica-air, in cases like this, is fibre extrusion [17] [18] [19]. We assemble and solve the associated eigenvalue problem, in the same manner as for the triangular and quadratic cases, including characteristic width analysis, to find stable solutions. The eigenvalues show a mode-splitting for the fundamental mode on the same order as for the triangular fibre, which may be accredited to similar symmetry effects as in the triangular cases.

This structure has the potential advantage over the studied triangular and quadratic lattice fibres with comparable core size, that the effective area of the fundamental mode is larger for this fibre, which may be explained by its lower air-filling fraction. We find that the increase in effective area of the fundamental mode is $[93, 58]\,\%$ for wavelengths $\lambda/\Lambda \in [0.25, 1.40]$. Although the increase is smaller than what was obtained for the increased core size, triangular fibre investigated earlier, the pentagonal structure, however, has an added advantage. When fibres are scaled to fit into systems with standard fibre radii ($\approx 5\mu m$ [20]) the absolute sizes of the air-holes in the pentagonal fibre become larger than in the

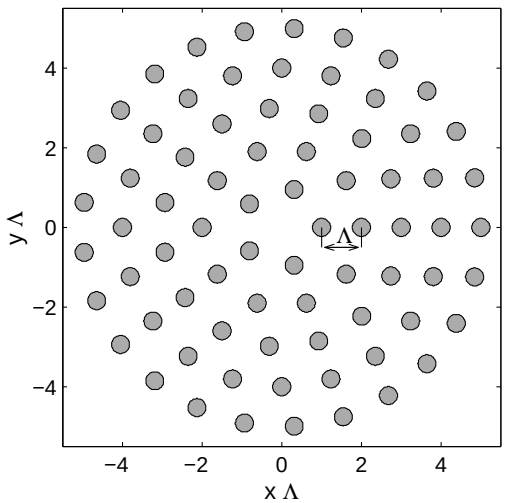

Figure 3.18: Schematic drawing of pentagonal 5-ring PCF, $d/\Lambda = 0.45$. No simple stacking pattern is evident

large core triangular fibre. Within reasonable limits, larger object sizes are easier to control precisely during draw. We also find that the increase in effective area is bought at the expense of coupling efficiency, $\eta_{pent.}$ (sec. 3.1.2), (to and from an optimally shaped Gaussian field (sec. 3.1)) which is $\eta_{pent.} \in [93, 96]\,\%$ of η_{tri}, and $\eta_{pent.} \in [87, 98]\,\%$ of $\eta_{tri,lg}$, where η_{tri} and $\eta_{tri,lg}$ denote coupling coefficients from a triangular small core fibre, and triangular large core fibre respectively, to an optimally shaped Gaussian field. The decreased coupling efficiency is hardly surprising considering the oddly shaped fundamental mode of the fibre (fig. 3.20).

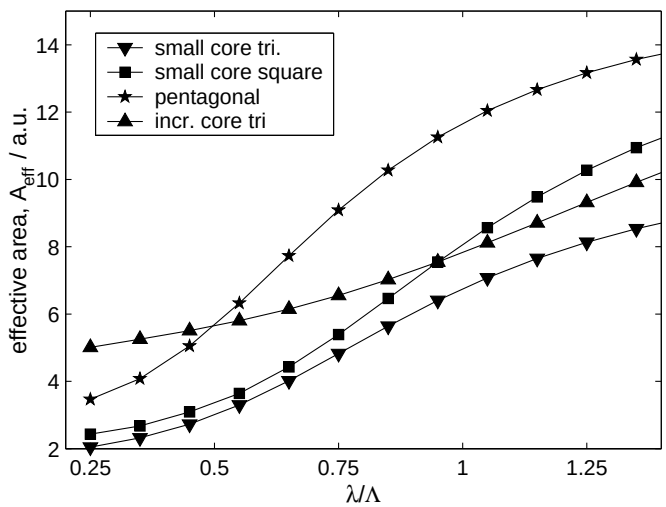

Figure 3.19: Effective area, A_{eff} (eq. 2.50) for a few different index guiding photonic crystal fibres, with $d/\Lambda = 0.30$.

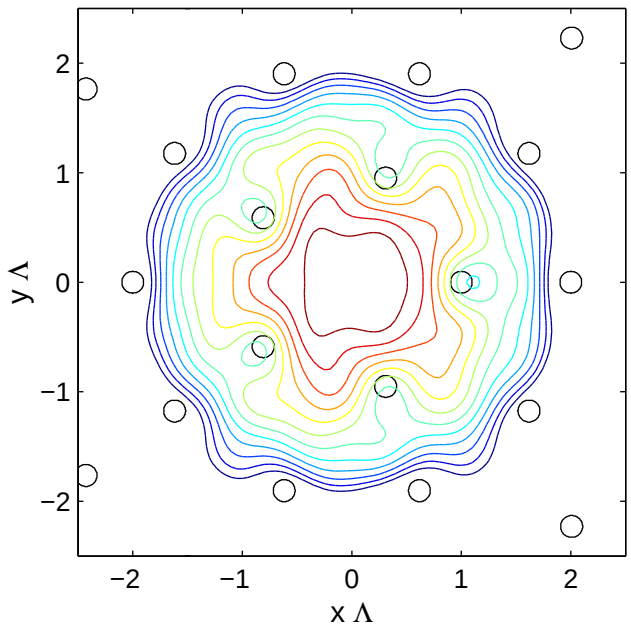

(a)

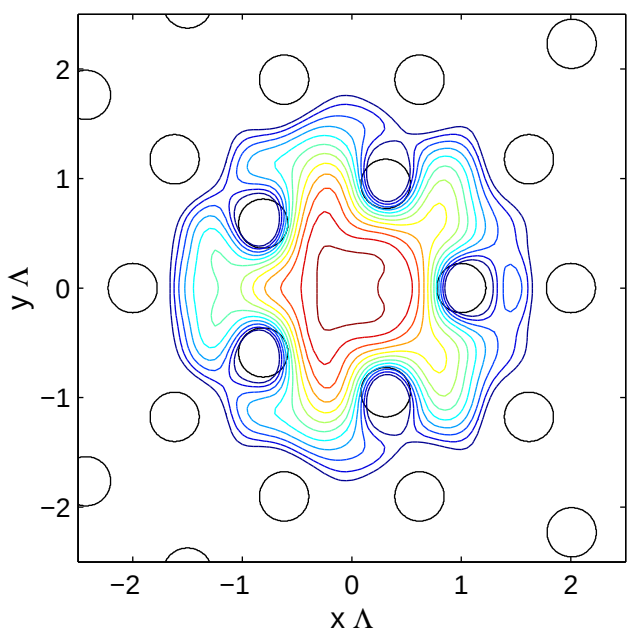

(b)

Figure 3.20: Squared magnetic field distribution of pentagonal 5-ring PCF, $d/\Lambda = 0.20 = 0.20$(a) ,0.45. (b), at $\lambda/\Lambda = 0.85$. Contours are spaced $2dB$ apart between $-2dB$ and $-24dB$.

3.4 Honeycomb photonic bandgap structure

As noted, inherent in the localised functions method is a difficulty in modelling photonic bandgap structures. The formation of photonic bandgaps depends on interaction between, in theory, a perfect crystal with an infinite number of periods, and the electromagnetic fields therein. As the restriction to a localised domain, limits this interaction, the usefulness of the proposed method is also limited by the forced localisation. Nevertheless, depending on the strength of the localisation of the defect modes, meaningful results can be obtained, especially when modelling fibres with finite, or small, cladding structures.

Photonic bandgaps do open in a triangular lattice structure [21] [22]. If the holes are not very large, however, the gaps tend to be narrow. Instead we consider the honeycomb structure (fig. 3.21), which inherently has larger bandgaps [23] [24]. This will serve as a case study to show that it is indeed possible to model bandgap structures with the Hermite Gaussian model[6]. For simplicity, we have not optimised the structures that we model in this section, instead the core hole is kept at the same size as the cladding holes, although bandgaps are wider for another configuration. The gaps have been shown to widen even further if targeted doping of the glass around the air-holes is used [25][7].

In a honeycomb configuration, the holes are situated on the corners of hexagons surrounding a central hexagon, in the centre of which the core defect is located. We define the size of the structure by the number of hexagon-rings surrounding a core. Thus, the structure in fig. 3.21 is a 3-ring structure. Our calculations were carried out for 3, 4, and 7 rings respectively. We set up the eigenvalue problem in the usual way and solve for eigenvalues and eigenvectors as before. Whereas, earlier, finding the eigenmodes of the fibre was a simple matter of sorting the eigenvalue by magnitude, the modes associated with a bandgap are expected to lie "sandwiched" between non-localised cladding modes. We also have to consider the possibility of "false" modes that become localised due to the forced localisation of the function series.

[6] Later on we shall use the Hermite Gaussian model where the plane wave method is not an option

[7] One way of achieving such a structure could be to use a CVD-process on a pre-stacked preform and deposit doped glass on the inner walls of the capillary tubes.

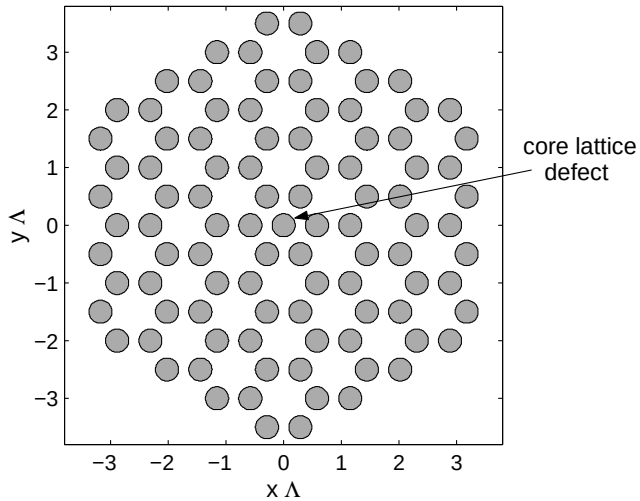

Figure 3.21: Schematic of a honeycomb cladding structure with $d/\Lambda = 0.40$. The lattice defect forming the core is the extra air-hole marked in the centre.

Taking the max-norm of the average difference between the j- and k-ring solution bands, $||\bar{\Delta}_{j,k}||_{max}$, to be a measure of convergence, we arrive at the conclusion, that with as few as 4 rings of hexagons, solutions are stable with respect to structure size. ($||\bar{\Delta}_{3,4}||_{max} < 10^{-3}, ||\bar{\Delta}_{4,7}||_{max} < 10^{-12}$)[8].

To find candidates for truly guided modes we solve the eigenvalue problem with (figs. 3.22 & 3.23, red) and without (fig. 3.22 & 3.23, black) the central core defect. By superimposing the modal indices we may find eigenvalues associated with the core, that are absent from the solutions of the homogeneous honeycomb structure. We identify two major gaps: The upper running from $\Lambda/\lambda < 1$ to $\Lambda/\lambda \approx 4.7$, the lower from $\Lambda/\lambda \approx 3.2$ to $\Lambda/\lambda > 8$. Two solutions associated with the defect, enter the upper gap at a $\Lambda/\lambda \approx 1.3$ (fig: 3.22, inset), but we find no defect associated solutions in the lower major gap. Upon closer inspection, we find a minor gap, centred around $\Lambda/\lambda \approx 1.7$, which has defect-associated modes traversing

[8] We are, of course, still limited by the same factors as seen earlier for index guiding fibres, resulting from the forced localisation. Thus, cladding modes cannot be expected to be properly resolved.

the bandgap. (fig 3.23). We also note that there is a non-core mode traversing this minor bandgap.

Thus far we have not discussed the impact of a change of characteristic width, ω_m, it is, as stressed before necessary to perform such an analysis to get useful results. Although varying ω_m is complicating the system further, we may turn it to our advantage by using a variational like argument: Any real mode which is not an artifact of the model, should be reproducible, to some extent, with $\omega_{m,0} + \delta\omega_m \; ; \delta << 1$, whereas other "false" solutions should vary strongly with the model parameters. Thus, the ambiguity of the characteristic width may help us sort out the wanted solutions. An analysis along these lines shows that the solutions in the upper major bandgap are unstable whereas the ones in the minor bandgap have counterparts for other values of ω_m.

Figure 3.24 shows intensity distributions in the minor bandgap. (fig. 3.23) Notice, for instance, the "doughnut" shape of the distribution in fig. 3.24(a), which agrees with the shape of a mode found using other means of calculation [23]. These solutions indicate that it is indeed possible, albeit rather complicated and with a need for many iterative calculations, to model photonic bandgap structures using the proposed Hermite Gaussian function method, bearing in mind that the validity of the solutions must be cross checked against variations in ω_m.

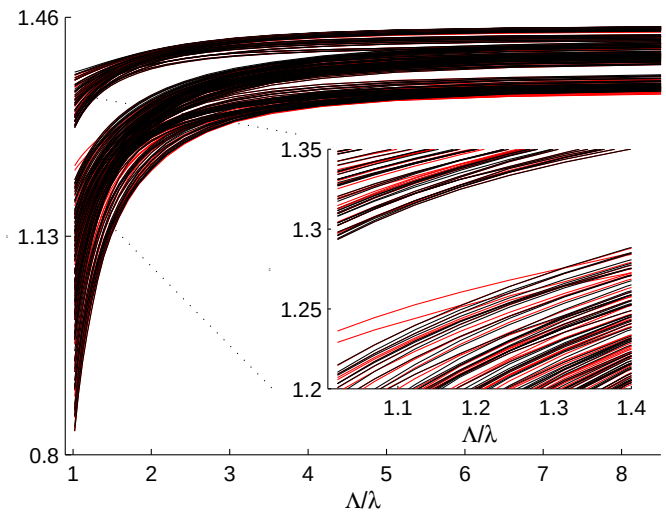

Figure 3.22: Eigenvalues of the first 144 solutions, for a honeycomb structure, $d/\Lambda = 0.40$, with (red), and without (black), core defect. The inset show two solutions entering the upper major bandgap.

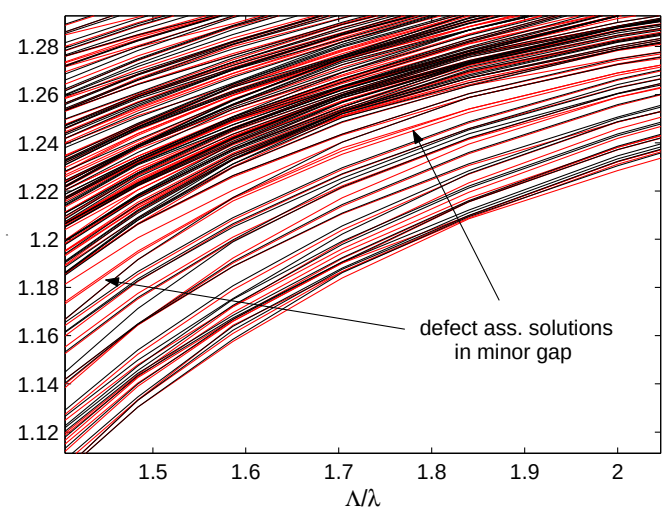

Figure 3.23: Close up of a minor bandgap among the first 144 eigenvalues (fig. 3.22), for a honeycomb structure, $d/\Lambda = 0.40$, with (red), and without (black), core defect.

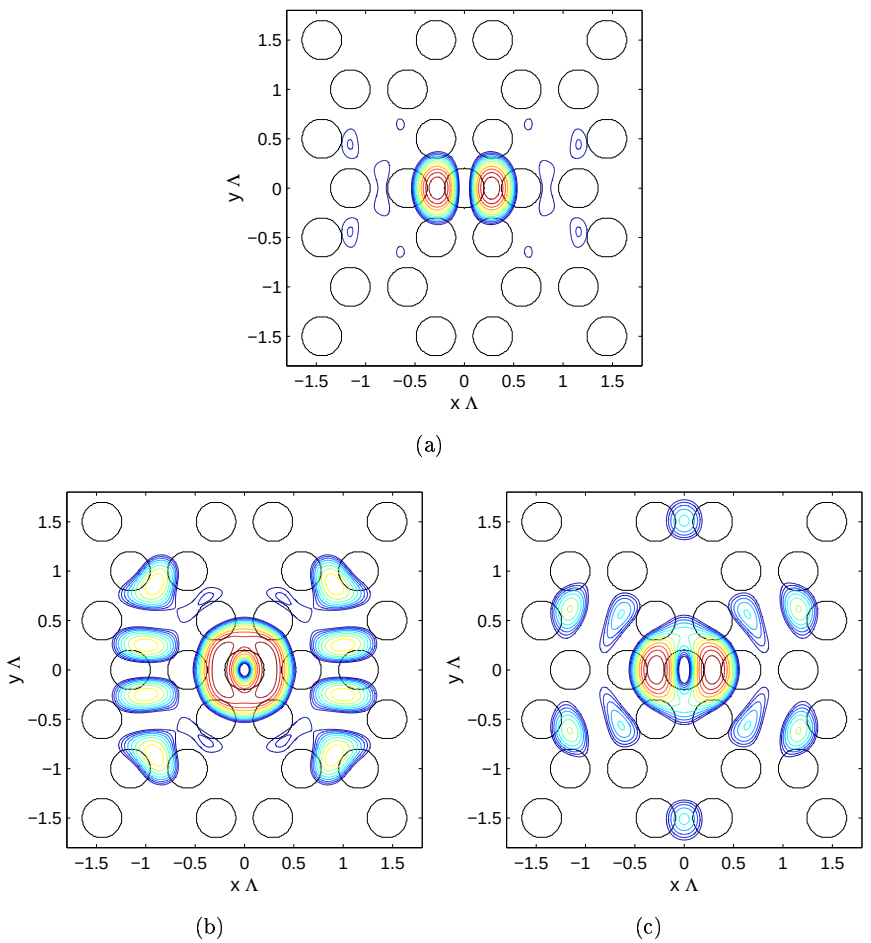

Figure 3.24: Squared magnetic field distributions for modes (eigenvalues nos. 124, 125 and 126 respectively), in the minor bandgap (fig 3.23) of a honeycomb photonic bandgap fibre with $d/\Lambda = 0.40$, for $\Lambda/\lambda = 1.48$. Contours range from $-2dB$ to $-24dB$ in $2dB$ steps.

3.5 Semi-periodic layered microstructured fibres.

In 1999 Fink et. al. [26] proposed an all dielectric version of the Bragg-fibre [27], the *omniguide*, where light is confined to the fire core by a Bragg-reflector which is "wrapped" around the core. If the refractive index variations of the dielectrics in the Bragg-reflector are tailored correctly an omnidirectional mirror may be formed [28][9]. At present, hollow core metallo-dielectric [29] fibres are used as delivery systems in high-power laser systems, such as CO_2-lasers in surgery, where silica cannot be used due to its extreme absorption in the far infrared range. A hollow core permits linear operation at high intensities, as well as a potentially lower loss than in dense material fibres since material absorption may be avoided. Therefore, hollow dielectric fibres have been suggested as a candidate for next generation transmission fibres [30].

Instead of directly making a Bragg-fibre with dielectrics of different refractive index, we may construct a fibre where the index steps are induced by arranging air-holes in concentric circles around a hollow core [1] (fig 3.25). Thus, we may retain the structural integrity of a fibre of undoped silica and air, while forming a Bragg reflector using effective indices of the structure. The design space of these fibre structures is massive, as the the hole-pattern within the concentric rings may be chosen freely, to fit whatever specifications might be wanted. As a starting point for future investigations we choose the two structures shown in fig. 3.25. They are relatively simple, and may be stacked, using large glass tubes to form high index rings and many small tubes to form the low index rings.

Using the same procedure as for the honeycomb photonic bandgap fibre, we may set up, and solve the eigenvalue problem defined by the structures, and search for solutions that meet criteria analogous to those in sec. 3.4. A fibre may be truly air-guiding if and only if, the index of a guided mode drops below the light-line [31][10]. A thorough investigation of the solutions obtained by the Hermite Gaussian method along the lines of sec. 3.4, reveals a doublet of modes in a narrow bandgap for both structures (figs. 3.26(a) and 3.27(a)). Using the obtained eigenvectors we calculate the electromagnetic field distribution of the bandgap modes, (figs. 3.26(b) and 3.27(b)) and find that the majority of the power carried

[9] For the omniguide a material system of Tellurium and polymers have been used.
[10] Defined by the dispersion relation for air.

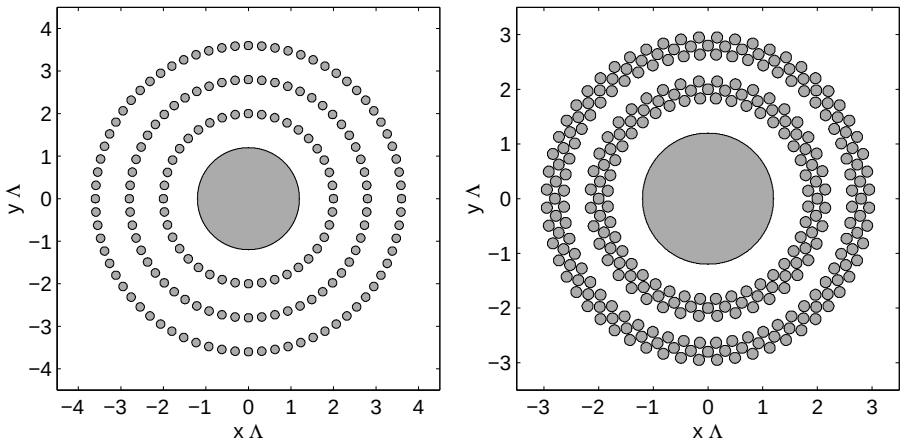

Figure 3.25: Schematic drawings of (a) hollow core, 3-ring, singlet, layered semi-periodic, and (a) hollow core, 2-ring, triplet, layered semi-periodic structure. (colloquially referred to as "onion"-fibres.)

by the modes, is indeed carried inside the hollow core. As expected the accompanying solutions (not shown) are degenerate with the ones shown with respect to a $\frac{\pi}{2}$-rotation. The fraction of power in air: $\rho = \frac{P_{air}}{P_{tot}} = 0.73$ for the singlet structure and $\rho = 0.84$ for the triplet structure. Compared with $\rho = 0.98$ obtained in an air-guiding triangular photonic crystal fibre (chapter 5), this it not impressive, but it may be remarked that these are the first (to the best of our knowledge) such fibre structures analysed, and no optimisation with respect to ρ has been attempted. As mentioned the design space is large, and a targeted search is expected to reveal much larger power fractions.

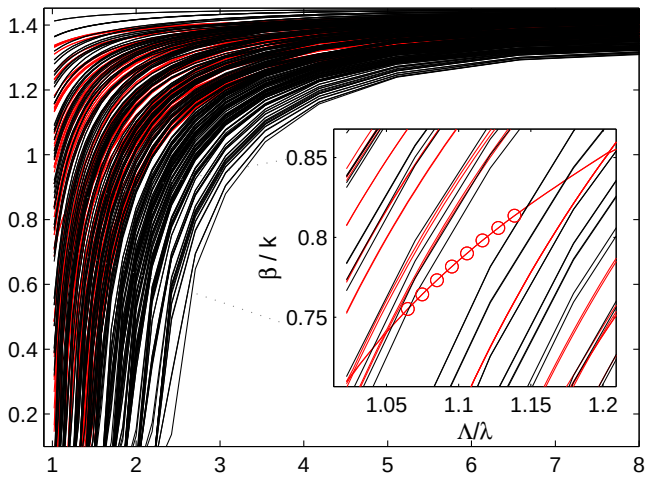

(a)

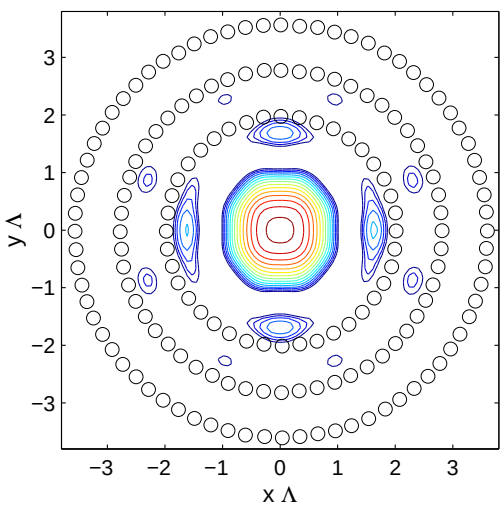

(b)

Figure 3.26: Modal indices (a) and field intensity contours (b) for an air-guided mode in a 2-ring single, layered structure. Contours range from $-2dB$ to $-32dB$ and are spaced $2dB$ apart. (fig. 3.25(a))

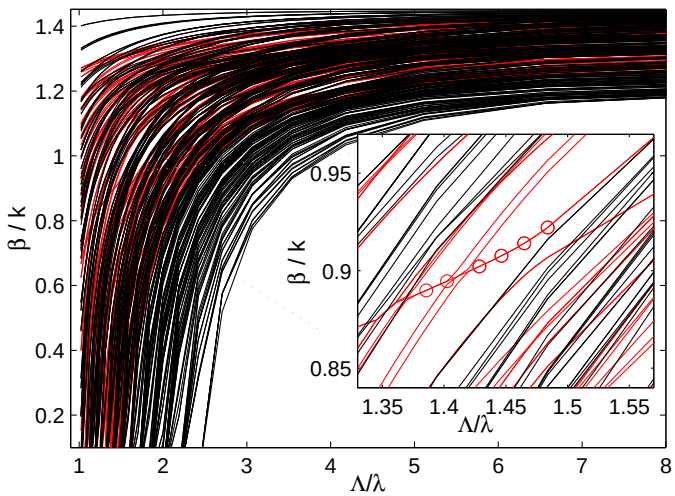

(a)

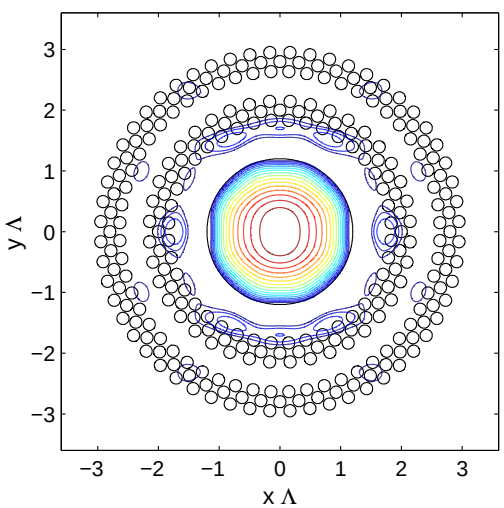

(b)

Figure 3.27: Modal indices (a) and field intensity contours (b) for an air-guided mode in a 2-ring triplet, layered structure. Contours range from $-2dB$ to $-32dB$ and are spaced $2dB$ apart. (fig. 3.25(b))

3.6 Summary of chapter 3

We have employed the modelling framework established in chapter 2 and used it to predict the properties of a range of different photonic crystal fibre structures, both index guiding and photonic bandgap fibres. As a starting point we have used the small core triangular fibre, which has been studied extensively in the literature. We have found that we may describe the general features of this fibre with the purely Hermite Gaussian model, using fairly short expansion series, if and only if the characteristic width of the function series is chosen carefully. We have also encountered limitations of the model, in terms of mode-field resolution, and erroneous splitting of degenerate modes. The first of which simply arises as an effect of the average mode-field diameter rising sharply with wavelength, eventually conflicting with the assumption of strongly localised fields, implied in the formulation in terms of Hermite Gaussian functions. The second is an effect of the expansion series not reflecting the symmetry of the underlying structure (in the triangular case six-fold rotational). Both effects may be counteracted at the expense of calculation time by using longer function series. To use a larger characteristic width is not feasible, since the interaction with small structural features may not be resolved properly. An investigation of a quadratic lattice crystal fibre did, in comparison, not show the splitting of degenerate modes.

We have calculated dispersion characteristics of the small core triangular fibre. These results agree with corresponding results in the literature, which have been obtained experimentally and with the standard localised function methods.

We have also investigated the possible gain, in terms of effective area and coupling efficiency, in a variant of the basic triangular fibre with an increased core size. We found an increase in effective area of up to a factor of 3, depending on hole size and wavelength. We have also investigated a novel pentagonal symmetry fibre, which may be advantageous over the large core fibre, although its manufacturing feasibility is unclear, and its effective area gain is smaller.

We have also applied our model to photonic bandgap structures: A honeycomb lattice structure and two layered semi-periodic "onion" structures. We have shown that it is possible, to model bandgap fibres with localised functions, although a lot of effort has to be made in examining

results, as "false" modes may appear on account of the forced localisation. Notable is that the first attempts at modelling the semi-periodic fibres show air-guided modes with an air-power fraction of 0.73 and 0.84 respectively.

References to chapter 3

[1] S. E. B. Libori, J. Broeng, A. O. Bjarklev, C. Rasmussen, and E. Knudsen. "Optical fibre for transmitting light, has improved polarization and dispersion properties, and includes microstructured cladding region surrounding core region." Patent, 2002. Number: WO200241050-A2, AU200223515-A.

[2] T. A. Birks, J. C. Knight, and P. S. Russel. "Endlessly single-mode photonic crystal fiber", *Optisc Letters*, vol. 22, no. 13, pp. 961–963, 1997.

[3] M. Midrio, M. P. Singh, and C. G. Someda. "The space filling mode of holey fibers: An analytical solution", *Journal of Lightwave Technology*, vol. 18, no. 7, pp. 1031–1037, 2000.

[4] F. A., E. Silvestre, J. J. Andres, P. Miret, and A. M. V. "Designing th eproperties of dispersion flattened photonic crystal fibers", *Optics Express*, vol. 9, no. 13, pp. 687–697, 2001.

[5] T. M. Monro, D. J. Richardson, N. G. R. Broderick, and P. J. Bennett. "Holey optical fibers. an efficient modal model", *Journal of Lightwave Technology*, vol. 17, no. 11, pp. 2078–2081, 1999.

[6] T. A. Birks, D. Mogilevtsev, J. C. Knight, P. S. Russel, J. Broeng, P. J. Roberts, J. A. West, D. C. Allan, and J. C. Fajardo. "The analogy between photonic crystal fibres and step index fibres", in *OFC/IOOC'99, volume 4,* pp. 114–116, 1999.

[7] J. Broeng, D. Mogilevtsev, S. E. Barkou, and A. Bjarklev. "Photonic crystal fibers: A new class of optical waveguides", *Optical Fiber Technology*, vol. 5, no. 3, pp. 305–330, 1999.

[8] M. J. Steel, T. P. White, C. M. de Sterke, R. C. McPhedran, and L. J. Botten. "Symmetry and degeneracy in microstructured optical fibers", *Optics Letters*, vol. 26, no. 8, pp. 488–490, 2001.

[9] ANSI/TIA. *FOTP-191 - IEC 60793-1-45 Optical Fibres - Part 1-45: Measurement Methods and Test Procedures - Mode Field Diameter (ANSI/TIA-455-191-B-2003)*, 2003.

[10] T. M. Monro, D. J. Richardson, N. G. R. Broderick, and P. J. Bennett. "Modelling large air fraction holey optical fibers", *Journal of Lightwave Technology*, vol. 18, no. 1, pp. 50–56, 2000.

[11] A. W. Snyder and J. D. Love. *Optical waveguide theory.* Kluwer Academic Publishers, 2000.

[12] D. Mogilevtsev, T. A. Birks, and P. S. Russel. "Group velocity dispersion in photonic crystal fibers", *Optics Letters*, vol. 23, no. 21, pp. 1662–1664, 1998.

[13] M. J. Gander, R. McBride, J. D. C. Jones, D. Mogilevtsev, T. A. Birks, J. C. Knight, and P. S. Russel. "Experimental measurement of group velocity dispersion in photonic crystal fibre", *EL*, vol. 35, no. 1, pp. 63–64, 1999.

[14] T. Sørensen, J. Broeng, A. Bjarklev, T. P. Hansen, E. Knudsen, S. E. B. Libori, H. Simonsen, and J. R. Jensen. "Spectral macrobending loss considerations for photonic crystal fibres", in *IEE Proceedings, Optoelectronics,* pp. 206–210, 2002.

[15] L. Farr, J. C. Knight, B. J. Mangan, and P. J. Roberts. "Low loss photonic crystal fibre", in *ECOC 2002, Post-deadline papers,* 2002.

[16] T. M. Monro, P. J. Bennett, N. G. R. Broderick, and D. A. Richardson. "Holey fibers with random cladding distributions", *Optics Letters*, vol. 25, no. 4, pp. 206–208, 2000.

[17] D. Furniss, J. D. Shephard, and A. B. Seddon. "A novel approach for drawing optical fibers from disparate core/clad glasses", *Journal of Non-Crystalline Solids*, vol. 213-214, pp. 141–146, 1997.

[18] D. J. Gibson and J. A. Harrington. "Extrusion method for fabrication of hollow waveguides with 1d-photonic bandgap structure", in *Proceedings of SPIE, volume #4616,* pp. 91–96, 2002.

[19] X. Quan. "Plastic optical fibers — pipe dream or reality?", in *Proceedings of the American Chemical Society, 'Polymer Preprints',* pp. 1279–1280, 1999.

[20] G. P. Agrawal. *Fiber-optic communication systems.* John Wiley and sons Inc., Third edition, 2002.

[21] T. A. Birks, P. J. Roberts, P. S. Russell, D. M. Atkin, and T. J. Shepherd. "Full 2-d photonic badngaps in silica/air structures", *EL*, vol. 31, no. 22, pp. 1941–1943, 1995.

[22] R. F. Cregan, B. J. Mangan, J. C. Knight, T. A. Birks, P. J. Russell, P. St.J. Roberts, and D. C. Allan. "Single-mode photonic band gap guidance of light in air.", *Science*, vol. 285, no. 5433, pp. 1537–1539, 1999.

[23] S. E. Barkou, J. Broeng, and A. Bjarklev. "Silica-air photonic crystal fiber that permits waveguiding by a true photonic bandgap effect", *Optics Letters*, vol. 24, no. 1, pp. 46–48, 1999.

[24] J. Broeng, S. E. Barkou, A. Bjarklev, J. C. Knight, T. A. Birks, and P. S. Russell. "Highly increased photonic band gaps in silica/air structure", *Optics Communications*, vol. 156, no. 4-6, pp. 240–244, 1998.

[25] J. Broeng, T. Søndergaard, S. E. Barkou, P. M. Barbeito, and A. Bjarklev. "Waveguidance by the photonic bandgap effect in optical fibres", *Journal of Optics A: Pure and Applied Optics*, vol. 1, no. 4, pp. 477–482, 1999.

[26] Y. Fink, D. J. Ripin, S. Fan, C. Chen, J. D. Joannopoulos, and E. L. Thomas. "Guiding optical light in air using an all-dielectric structure", *Journal of Lightwave Technology*, vol. 17, no. 11, pp. 2039–2041, 1999.

[27] P. Yeh, A. Yariv, and E. Marom. "Theory of a bragg fiber", *Journal of the Optical Society of America*, vol. 68, no. 9, pp. 1196–1201, 1978.

[28] Y. Fink, J. N. Winn, S. Fan, C. Chen, J. Michel, J. D. Joannopoulos, and E. L. Thomas. "A dielectric omnidirectional reflector", *Science*, vol. 282, no. 5394, pp. 1679–1682, 1998.

[29] J. A. Harrington. "An overview of power delivery and laser damage in fibers", in *Proceedings of SPIE, volume #2966,* pp. 536–544, 1997.

[30] S. G. Johnson, M. Ibanescu, M. Skorobogatiy, O. Weisberg, T. D. Engeness, M. Soljacic, S. A. Jacobs, J. D. Joannopoulos, and Y. Fink. "Low-loss asymptotically single-mode propagation in large-core omniguide fibers", *Optics Express*, vol. 9, no. 13, pp. 748–779, 2001.

[31] J. D. Joannopoulos, R. D. Meade, and J. N. Winn. *Molding the flow of light.* Princeton University Press, 1995.

Chapter 4

Modelling of microbend induced losses in photonic crystal fibres

Microbends in optical fibres are statistical variations in the geometry of an optical fibre, introduced in the fabrication process. The bend radii of these bends are, by nature, generally much larger than for macrobends (chapter 5, and the loss in each bend significantly lower. On the other hand, the number of microbends is expected to be much higher than that of macrobends. In the microbend case the main source of loss is transition loss - not radiation loss. A bend deforms the mode[1] and introduces a mismatch with the undeformed mode. As modes in PCFs are not generally circularly symmetric the mode mismatch may depend on the direction in which the fibre is bent.

In this chapter we present an approach toward predicting microbend induced transition losses, by considering the statistical distribution of curvature transitions in fibres.

4.1 Model

If the bend is sufficiently small, a bent conventional optical fibre may be modelled by an equivalent straight fibre with a a slope, or tilt, in the direction of the bend, added to the refractive index profile of the fibre [1]. This procedure is also applicable to the Hermite Gaussian formulation (chapter 2) in a straight forward manner, by adding a linear term in x and/or y to eq. 2.27.

$$\epsilon(x,y) = \epsilon_{bg} + (b_x x + b_y y) \sum_j (\epsilon_j - \epsilon_{bg}) \sum_{f,g}^{D} c_{f,g}^j \psi_{f,g}^{\omega_d^j}(x - r_x^j, y - r_y^j) \quad (4.1)$$

where b_x and b_y are slope constants in x and y-directions. The overlap integrals involved in transforming eq. 2.2 and 2.3 to eq. 2.9 are bounded due to the strong localisation of the Gaussian function, and are easily evaluated using a recursion formula (eq. 2.21. Given b_x and b_y, we can solve the eigenvalue problem as before and calculate electromagnetic fields, in a photonic crystal fibre with a tilted dielectric function.

Thus, we evaluate the transition loss between two fibre segments with different bend radii, using the coupling equation (eq. 2.47). Through a weighted summation of such transitions between fibre segments, we

[1] Pushes its centre of gravity in the opposite direction of the bend.

compute a mean transition loss, where the weight function is derived from statistical properties of the microbends describing the probabilities for the occurrence of each transition.

Implied in this argumentation is the assumption that the power fraction reflected at an interface is lost. In principle, a photon reflected at a radius-transition at z_k may be trapped in a backward travelling mode, in which case it may also be re-reflected back into a forward travelling mode at any of the preceding transitions $z_j < z_k$. This subjects the photon to a delay of $t \geq 2\frac{z_k - z_j}{c}$. For transmission purposes, due to the statistical nature of the bends, such photons would not contribute constructively to a transmitted signal, wherefore we will, in the following, regard it as being lost.

4.1.1 Curvature model

We model the axial fibre displacement, $d(z)$, of the fibre as a Gaussian stochastic process [2] [3] with mean zero and covariance function $g(\tau); \tau = z_2 - z_1$ This ensures that, given a four times differentiable covariance function, we may differentiate the process itself two times. This facilitates the use of a standard formula for curvature,κ, of a function on one variable, $f(t)$ [4]:

$$\kappa_f = \frac{1}{r_f} = sgn(\frac{d^2 f}{dt^2}) \frac{|\frac{d^2 f}{dt^2}|}{(1 + (\frac{df}{dt})^2)^{3/2}} \tag{4.2}$$

where $sgn(\frac{f^2 f}{dt^2})$ is the sign of $\frac{f^2 f}{dt^2}$ and r_f is the curvature radius[2]. A differentiated Gaussian process, $\frac{dX\{t\}}{dt}$, is also itself a Gaussian process and, therefore, at any given point t, uncorrelated with the undifferentiated process at t [5]. Thus, we may consider the curvature a stationary stochastic process as a quotient of two uncorrelated stationary processes where the numerator is a Gaussian process and the denominator a function of a χ^2-process [6]. Using standard formulae for uncorrelated stochastic variables [5], we may express the momentary distribution function of the

[2]The derivation of eq. 4.2 requires $fracd^2 f dt^2$ to be either positive or negative — the factor $sgn(\frac{d^2 f}{dt^2}) \cdot |\frac{d^2 f}{dt^2}|$ may as well be lumped in the numerator.

curvature as:

$$P\left(\kappa(z) < \zeta\right) = F_{\kappa(z)}(\zeta) = \int_1^\infty F_{d''(z)}(\zeta y)\frac{2}{3g''(0)y^{1/3}} f_{d'(z)}\left(\frac{(y-1)^{2/3}}{g''(0)}\right) dy \tag{4.3}$$

where f_X denotes the probability density function and F_X the distribution function of the stochastic variable X. This integral has no simple solution — we therefore rely on an adaptive numerical integration scheme [7] for its evaluation.

4.1.2 Displacement process

The properties of the fibre displacement process is dependent on the environment the fibre is subject to. We choose to focus on a known scheme in order to compare our results to those obtained for step index fibres. This scheme describes the situation where an outer disturbance is pressed against the fibre. This is applicable when an irregular fibre coating, or jacket, is put around the fibre. Following Gloge [8], we write the power spectrum of $d(z)$ as:

$$G_d(s) = \frac{1}{(1+l^2s^2)^3}\frac{\sigma^2}{(1+\frac{H}{D}s^4)^2} \tag{4.4}$$

Here s denotes frequency, l and σ denote the correlation length and the standard deviation of the outer disturbance pressed against the fibre, such as an irregularly thick coating. H and D represent the stiffness (Young's moduli) of fibre and coating material, respectively. Although, this form is valid under the assumption that there is complete, continuous contact between fibre and coating, effects of incomplete contact may readily be included within the framework of this model, by a straightforward extension [8]. Disallowing discontinuous contact is expected to result in an overestimate of the losses for stiff contact materials, but also requires that the pressing force be considered.

Other types of covariance functions have been suggested, such as an oscillating exponential [9]. We choose the form of eq. 4.4, since it it may be derived directly from the mechanics of bending of a thin beam, whereas, as the production of PCFs is still in its infancy, statistical data for microbends are bound to be unreliable. Hence the decision to rely

solely on basic theoretical assumptions. Even so, this is a flexible model, which may easily be extended to evaluate the effect on microbending of, for instance, fibre bundling.

Given the power spectrum we may now calculate the curvature distribution for given fibre parameters. Using the stiffness of silica, 7000 kg/mm^2, for the fibre and some different materials for the jacket we evaluate the probability density function for a disturbance with standard deviation, $\sigma = 1\,\mu m$ and correlation length, $l = 1\,mm$ (fig. 4.1).

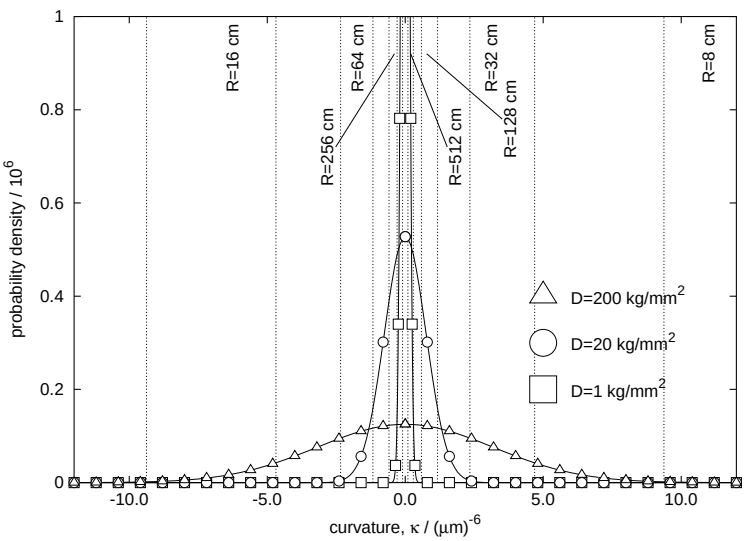

Figure 4.1: Probability density functions of the curvature of a fibre in contact with jacket materials of varying stiffness. The roughness of the surface is described by a standard deviation, $\sigma = 1 \cdot 10^{-6}$ and a correlation length, $l = 0.001m$

4.1.3 Coupling coefficients

We calculate the electromagnetic fields using the Hermite Gaussian model (chapters 2 and 3) in a curved fibre, with bend radius r, through an equivalent straight fibre with a tilted refractive index profile as [10] [11]:

$$\epsilon = \epsilon_{str.} + \frac{2\pi}{r}x \Rightarrow b_x = \frac{2\pi}{r} \tag{4.5}$$

assuming the fibre to be bent in the x-direction only [3]. Modal fields calculated in a triangular lattice, small core fibre (chapter 3, sec. 3.1) with a tilted index profile are shown in fig. 4.2.

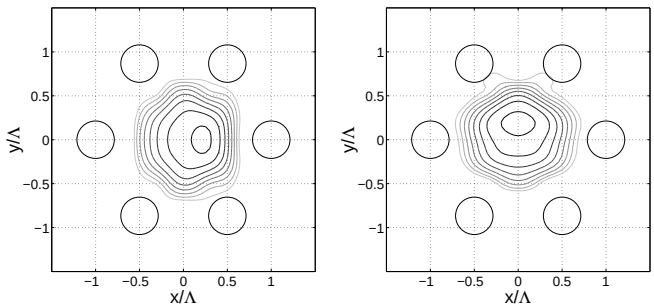

Figure 4.2: Magnetic field of a photonic crystal fibre with $d/\Lambda = 0.45$, bent in the two principal directions. (an excessively small bend radius is used to emphasise the displacement of the field)

Using eq. 2.47 and two sets of Hermite Gaussian expansion series, obtained as eigenvectors from fibre segments with different curvatures, we calculate coupling coefficients, $\eta_{r_1 \to r_2}$, for a set of radius-transitions in a triangular PCF (fig. 4.3).

We now write an averaged momentary coupling coefficient, $\bar{\eta}(\lambda, \tau)$, as

$$\bar{\eta}\left(\lambda, \tau\right) = \int_{r_1=-\infty}^{\infty} \int_{r_2=-\infty}^{\infty} \eta_{r_1 \to r_2} \cdot P\left(r(z_2) = r_2 \mid r(z_1) = r_1\right) dr_1 dr_2 \tag{4.6}$$

where $P\left(r(z_2) = r_2 \mid r(z_1) = r_1\right)$ denotes the probability of a transition between the bend radii r_1 and r_2 in the interval $]z_1, z_2[$, and $\eta_{r_1 \to r_2}$ the coupling coefficient between electromagnetic fields in fibre segments with bend radii r_1 and r_2 respectively. As noted $\eta_{r_1 \to r_2}$ may readily be calculated through the expansion coefficients of the Hermite Gaussian description of the fields in index profiles tilted appropriately.

Averaging the coupling coefficients, $\bar{\eta}(\lambda, \tau)$, over the length of the fibre we get a total mean coupling coefficient only dependent on wavelength as:

$$\bar{\eta}(\lambda) = \lim_{L \to \infty} \frac{1}{L} \int_0^L \bar{\eta}\left(\lambda, \tau\right) d\tau \tag{4.7}$$

[3] Bending in another direction is, of course, completely analogous

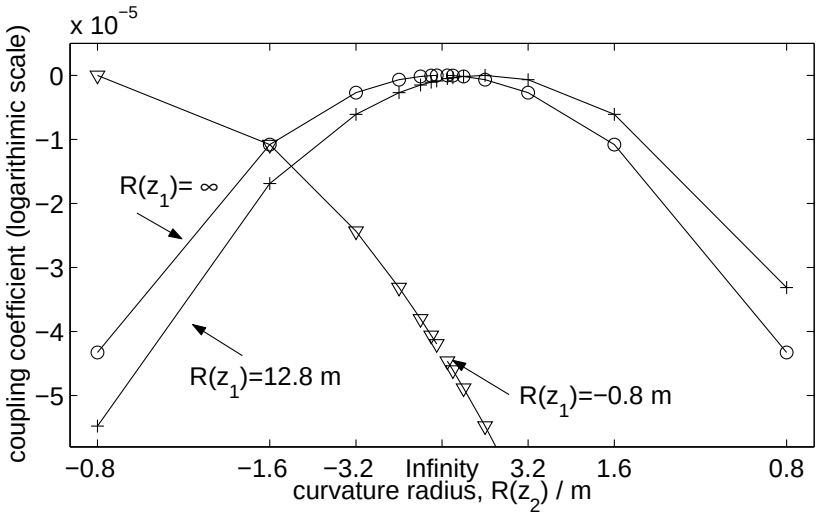

Figure 4.3: Coupling coefficients for some curvature transitions at a wavelength of $\lambda = 1.25\mu m$, Fibre is bent in the x-direction.

If $\lim_{\tau\to\infty} g(\tau) = 0$ we approach a steady state solution where the two instances $d(z_1)$ and $d(z_2)$ are uncorrelated. The weighting probabilities in eq. 4.6 may then be calculated using eq. 4.4 in eq. 4.3.

In order to numerically evaluate the integral (eq. 4.6) we assume the coupling coefficients to be piecewise constant, and so replace the integral with a summation

$$\bar{\eta}\left(\lambda,\tau\right) = \eta_{r_1\to r_2} \sum P\left(r_{2a} < r(z_2) < r_{2b} \mid r_{1a} < r(z_1) < r_{1b}\right) \qquad (4.8)$$

The intervals used in our calculations are indicated in fig. 4.1. According to fig. 4.3, assuming coefficients to be constant in the larger, "outer" intervals, is a crude approximation. In the cases investigated here, however, transitions to and from the outermost intervals are correspondingly unlikely (fig. 4.1). Hence, the "outer" contributions to the mean loss factor are correspondingly small, justifying the approximation.

4.2 Microbend loss factor

Once the mean coupling coefficient has been calculated it may expressed as a microbending loss factor or mean loss. We have performed these calculations on a triangular fibre structure with a lattice spacing, $\Lambda = 1.0\mu m$ and then evaluated the mean coupling losses as a function of wavelength. The lattice has two principal directions in which the holes closest to the fibre core, are in the $\frac{\pi}{3}$ rotational group of the x-direction (fig. 4.2) and the farthest holes are in the y-direction or its associated rotations.

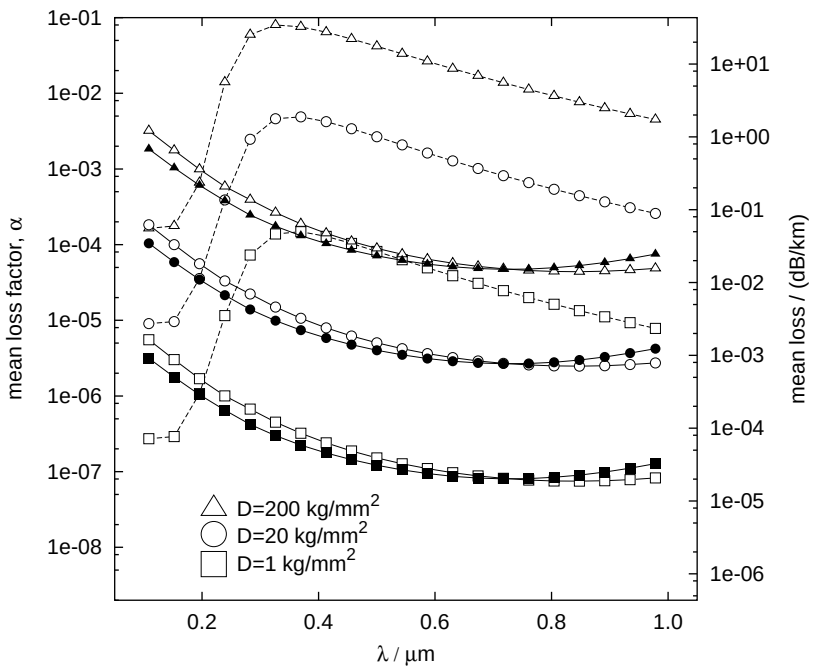

Figure 4.4: Mean transition loss for fibres with three different jacket materials. Solid curves: PCF with microbends in (solid symbols) x-direction and (open symbols) y-direction. Dashed curve: Step index fibre, with similar index contrast, with microbends in one direction. For $\lambda > 0.5$ the mode field diameter rises sharply (in the step index fibre) — fields are not resolved well.

We therefore expect these directions to form bounds for one-dimensional

microbend induced transition losses. Figure 4.4 shows the predicted mean loss factor in the two directions. Also, as a comparison we have performed the same analysis on a step index fibre with an index contrast similar to the effective index contrast of the PCF [12]. Firstly, The PCFs show, under the assumptions of the model, a significantly different spectral behaviour. Secondly, is apparent that PCFs do not show significantly higher losses due to overall microbends compared to step index fibres, on the contrary. Thirdly, the calculations imply that curvature transition losses caused by microbends may be efficiently avoided by using a soft coating material. In this case non-uniformities in the coating tend to be absorbed by the softer material rather than affect the fibre.

As mentioned above the reported model may be extended by allowing discontinuous contact between fibre and surrounding medium. Extensions allowing bends in all directions and/or twists in the fibre are also possibilities within the framework of the stochastic process approach we have employed.

4.3 Summary of chapter 4

In chapter 4 we have presented a technique for modelling microbend induced losses in photonic crystal fibres. By regarding the displacement of the fibre core, generating the microbends, as a stationary Gaussian process and regarding coupling losses between fibre segments of different curvature, we have calculated a mean loss factor for the fibre. Results imply that index guiding photonic crystal fibres have significantly different spectral characteristics when compared with step index fibres, and that overall microbends do not explain the comparatively higher losses found in PCFs. We have also not found any major difference between microbending loss factors, associated with bends being oriented in either of the two principal lattice directions of the fibre.

References to chapter 4

[1] A. W. Snyder and J. D. Love. *Optical waveguide theory.* Kluwer Academic Publishers, 2000.

[2] J. Sólnes. *Stochastic processes and random vibrations, theory and practice.* John Wiley and sons Inc., 1997.

[3] J. Møller. *Aspects of spatial statistics, stochastic geometry and Markov chain Monte Carlo methods.* Department of Mathematical Sciences, Aalborg University, 1999.

[4] L. Hellström, S. Morander, and A. Tengstrand. *Envariabelanalys.* Studentlitteratur, 1991.

[5] G. Lindberg and H. Rootzén. *Stationära stokastiska processer.* Lund Institute of Technology, Fourth edition, 1994.

[6] G. Blom. *Sannolikhetsteori med tillämpningar.* Studentlitteratur, 1984.

[7] "Gnu scientific library, gsl". Http://www.gnu.org/software/gsl/.

[8] D. Gloge. "Optical-fiber packaging and its influence on fiber straightness and loss", *Bell Systems Technical Journal*, vol. 54, no. 2, pp. 245–262, 1975.

[9] K. J. Blow, N. J. Doran, and S. Hornung. "Power spectrum of microbends in monomode optical fibres", *Electronics Letters*, vol. 18, no. 11, pp. 448–450, 1982.

[10] R. L. Goyal, I. C. Gallawa and A. K. Ghatak. "Ben planar waveguides and whispering gallery modes: A new method of analysis", *Journal of Lightwave Technology*, vol. 8, no. 5, pp. 768–774, 1990.

[11] J. C. Bagget, T. M. Monro, K. Furusawa, and D. J. Richardson. "Distinguishing transition and pure bedn losses in holey fibers", in *CLEO'02,* pp. 49–50, 2002.

[12] T. A. Birks, D. Mogilevtsev, J. C. Knight, P. S. Russel, J. Broeng, P. J. Roberts, J. A. West, D. C. Allan, and J. C. Fajardo. "The analogy between photonic crystal fibres and step index fibres", in *OFC/IOOC'99, volume 4,* pp. 114–116, 1999.

Chapter 5

Macrobending loss-estimation of air-guiding photonic crystal fibre

By using a photonic bandgap fibre with a large air-filling fraction in the cladding region, Cregan et. al. in 1999 [1] demonstrated an air-guiding fibre with the property of guiding most of the optical power in a large air-filled core region. A very similar crystal fibre design was suggested and theoretically analysed by Broeng et. al. [2] indicating that the power fraction propagating in the air-filled core could be as high as 98%.

One of the obvious consequences of the photonic bandgap wave-guiding properties is a different kind of spectral sensitivity towards macrobends. For the effective deployment of air guiding fibres as transmission fibres it is of vital importance to characterise them in terms of macrobending loss behaviour. This spectral response may also be of great interest for sensory applications. In this chapter we will present a means of estimating macrobending losses in photonic bandgap fibres.

5.1 General characteristics and mode calculation

Whenever an optical fibre is bent, some fraction of the transported power will be radiated from the fibre core. This is the main source of loss when considering macrobend losses. In a geometric optic description, the fraction of electromagnetic fields on the outer side of the bend, must travel faster in order to "keep up" with the wavefront. The fractions of the fields that need to exceed the speed of light will be radiated from the mode. A mode's concentration to the core, and hence the magnitude of its macrobending loss, depends strongly on the index contrast between core and cladding. The fundamental mode of a standard optical fibre, contracts monotonically to the core with decreasing wavelength, leading to a single, long wavelength loss edge. As noted earlier, (chapter 3), an index guiding PCF exhibits a very different behaviour. As the effective index of the cladding [3] [4] is wavelength dependent, and approaches that of the core as the frequency increases, a second, short wavelength, macrobending loss edge is present.

The picture is less clear for a photonic bandgap fibre. In contrast to a real step index fibre, which has one single long wavelength, cutoff wavelength, a photonic crystal fibre operating by the photonic bandgap principle, will have two cutoff limits, i.e. the bandgap edges, defining a wavelength interval in which a mode may be guided. This is indicated in fig. 5.1, in which the photonic bandgap of the triangular cladding structure

is shown, limited by the upper and lower bandgap edges. A full analysis of the large-core photonic bandgap fibre reveals the presence of a degenerate core mode, and the small circles show the trace of these modes for a normalised propagation constant interval from $\beta\Lambda = 8.4$ to $\beta\Lambda = 9.15$. Within the bandgap, the mode is confined within the air-core. Hence, the leakage-free operational window of bandgap fibres is determined as the spectral range for which the mode is positioned inside the photonic bandgap. Outside the bandgap, the mode becomes resonant with allowed cladding modes, and for a real (finite) fibre it must, therefore, be considered leaky. For a relatively broad spectral range, however, the leaky mode retains its maximum within the air-core.

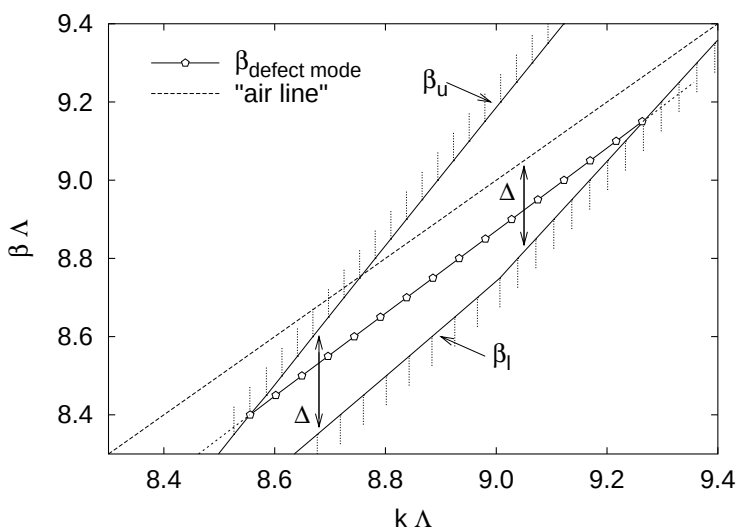

Figure 5.1: Photonic band structure diagram for a silica-air, triangular photonic crystal fibre with an air-filling fraction of 70%, and a core region formed by the removal of seven central holes as illustrated in fig. 5.2. By the circles, the band of the fundamental guided mode is indicated as it traverses the band gap. The dashed line is the air-line where $\beta = k$. The two deltas represent the two ways of determining the relative index difference.

5.2 Macrobending loss estimation

We analyse the mode-propagation properties of the air-guiding photonic crystal fibres, by employing a plane-wave expansion method [5] [2] [6]. An example of the air-guiding fibre structure analysed is shown in fig. 5.2, where also the contour curves for the squared magnetic field distribution of the guided mode are illustrated.

The fundamentally different properties of standard optical fibres versus those of photonic bandgap fibres, also reflect on the way to determine the macrobending loss. A full analysis of these properties, forms an intensive computational task. In order to make a first estimate of the macrobending losses, we have chosen a simpler approach, in which a well-proven bending loss formula for standard optical fibres is applied [7] (eq. 5.1).

$$\frac{P_r}{P_q} = 2\alpha = \frac{\sqrt{\pi}A_e^2}{4P} \frac{a \exp\left(\frac{-4\Delta w^3}{3av^2}R\right)}{w\left(\frac{wR}{a} + \frac{v^2}{2\Delta w}\right)^{1/2}} \tag{5.1}$$

where R is the radius of the bend investigated.
To apply the formula we must express some key elements, in terms of analogies between the step index fibre and the photonic bandgap fibre. In a step index fibre, the modal index of a guided mode is bounded by the core- and cladding refractive indices, and the mode's confinement is governed by the contrast, Δ, between these indices. A photonic bandgap mode, on the other hand, is bounded by the modal indices of the permitted cladding modes on the edges of the bandgap (or the zero dispersion, air line [8] if it lies within the bandgap). It is therefore natural to define Δ, as the difference between the upper and lower bandgap edges, β_u and β_l respectively (fig. 5.1), or as the difference between the air line and β_l where the it lies within the bandgap. As modes become leaky on either side of the bandgap, we have chosen to let the the refractive index of the cladding be defined by the bandgap edge closest to the propagating mode. Following this analogy, we identify the following parameters of the formulation (eq. 5.1):

- The effective v-parameter $v = v_{eff}$ [3][1].

[1] Known in the conventional fibre community as normalised frequency

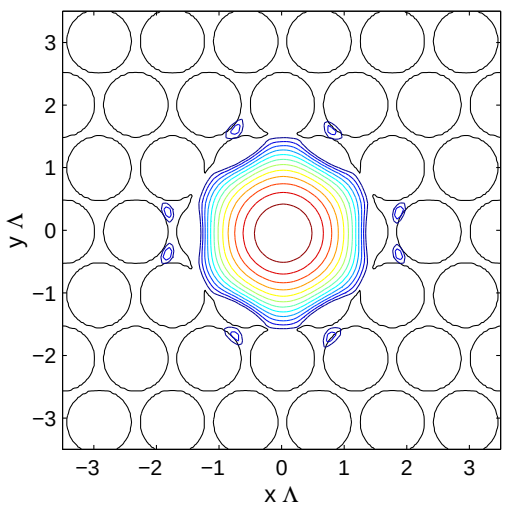

Figure 5.2: Air-guiding photonic bandgap fibre structure. The cladding structure is triangular with a pitch $\Lambda = 1.1\mu m$ and a relative hole diameter $d/\Lambda = 0.9$. Also shown are the contour curves of the squared magnetic field distribution of the guided mode calculated at a wavelength of $1.55\mu m$.

- The cladding propagation factor, $w = a(\beta^2 - \beta^2_{cladding})$, where a is the core radius of the fibre, and $\beta_{cladding}$ is β_l, β_u or the air line — whichever is closer to to the mode. a is estimated through the effective v-parameter, yielding $a = 0.625\Lambda$.

- the coefficient of the modified Bessel-function describing the field in the cladding of a step index fibre, A_e.

- the total power carried in the mode, integrated over the fibre cross section,P.

For added simplicity we have also used a Gaussian field approximation, which greatly simplifies the representation of the ratio A_e^2 to P [9].

5.3 Macrobending loss properties of air-guiding fibres

With the above described formulation we calculated the macrobending losses for a number of different wavelengths for two principal directions shown in figure 5.3. A Gaussian field was fitted to each field distribution to simplify the calculation of the macrobending loss. The tails of the field distribution vary somewhat for the two directions, but are otherwise very similar.

Results of our bending loss calculations are shown in figure 5.3 where we have used a fibre designed to transmit power at a wavelength of $\lambda = 1.55\mu m$. Note that both principal directions are plotted in figure 5.3. Thus, we conclude that the macrobending loss function (under the given simplifications) is comparatively insensitive to the directional field variations we see in figure 5.3. A further numerical analysis of the elements of eq. 5.1 shows that the exponential function in the numerator is the overall dominating factor, which yields the "on-off"-like behaviour.

In comparison, we have attained macrobending loss data for a standard, step index fibre[2], and compared them to the calculated loss function of the air-guiding fibre (fig. 5.3). Clearly the slopes of the air-guiding fibre's loss function are very much steeper. In a practical sense we obtain a transmission window $\approx 100nm$ wide. This very steep slope may for

[2] Chosen such that the loss edges coincide.

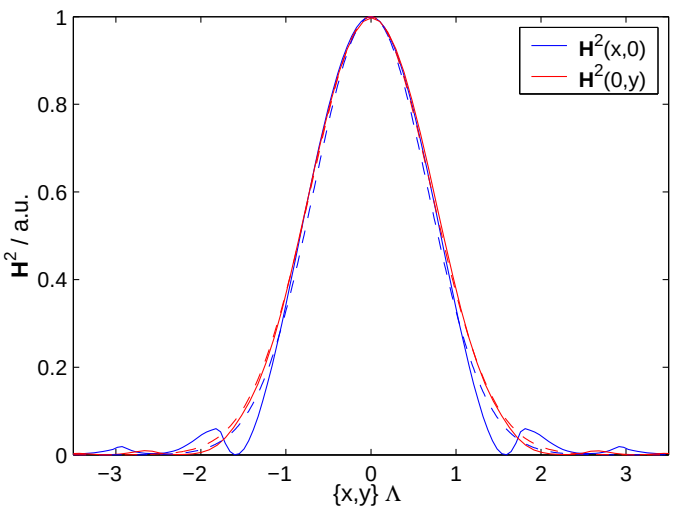

Figure 5.3: The squared magnetic field in two principal directions of the silica-air, triangular crystal fibre with air filling fraction of 70%, and core region as depicted in fig. 5.2. The solid lines represent the calculated fields, the dashed the fitted gaussians. The x-direction and y-direction are represented by blue and red lines respectively.

instance be used to differentiate wavelengths as the difference between a radiated, and a transmitted wavelength is on the order of $10nm$.

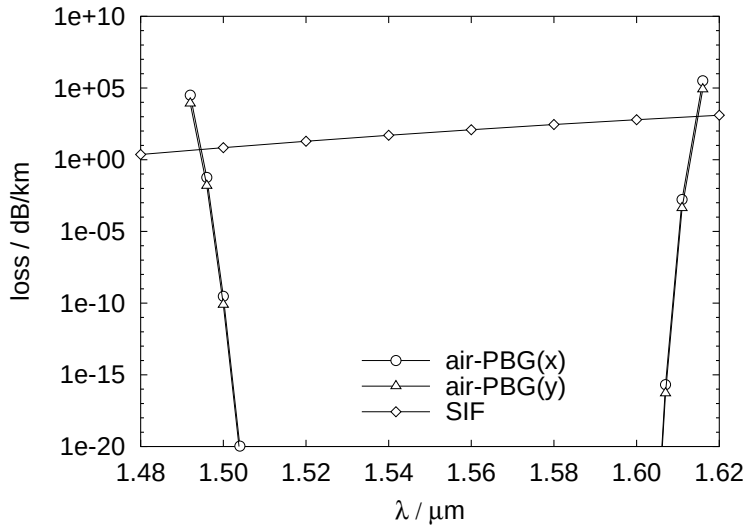

Figure 5.4: Macrobending loss versus wavelength for two principal directions for an air-silica photonic crystal fibre. Bending radius is $3cm$. Circles and triangles correspond to the photonic bandgap fibre, diamonds to a standard step index fibre.

5.4 Summary of chapter 5

We have presented an analysis of macrobending losses in air-guiding photonic crystal fibres. The analysis shows that such fibres, as opposed to standard optical fibres, show two bending loss flanks, in effect creating a transmission band, in which optical power is transmitted with very little appreciable bending loss regardless of bending radius. The slopes of the loss-flanks are radically steeper than the slope of the bending loss function encountered in standard fibres — the difference between a transmitted and a radiated wavelength is on the order of $10nm$ facilitating a means of differentiating between two wavelengths, which may be of use for sensory applications.

References to chapter 5

[1] R. F. Cregan, B. J. Mangan, J. C. Knight, T. A. Birks, P. J. Russell, P. St.J. Roberts, and D. C. Allan. "Single-mode photonic band gap guidance of light in air.", *Science*, vol. 285, no. 5433, pp. 1537–1539, 1999.

[2] J. Broeng, S. E. Barkou, A. Bjarklev, and T. Søndergaard. "Analysis of air-guiding photonic bandgap fibers", *Optics Letters*, vol. 25, no. 2, pp. 96–98, 2000.

[3] T. A. Birks, J. C. Knight, and P. S. Russel. "Endlessly single-mode photonic crystal fiber", *Optisc Letters*, vol. 22, no. 13, pp. 961–963, 1997.

[4] J. Broeng, D. Mogilevtsev, S. E. Barkou, and A. Bjarklev. "Photonic crystal fibers: A new class of optical waveguides", *Optical Fiber Technology*, vol. 5, no. 3, pp. 305–330, 1999.

[5] R. D. Meade, A. M. Rappe, K. D. Brommer, J. D. Joannopoulos, and O. L. Alerhand. "Accurate theoretical analysis of photonic band-gap materials", *Physical Review B*, vol. 48, no. 11, pp. 8434–8437, 1993.

[6] S. G. Johnson and J. D. Joannopoulos. "Block-iterative frequency domain methods for maxwell's equations in a planewave basis", *Optics Express*, vol. 8, no. 3, pp. 173–190, 2001.

[7] J. Sakai and T. Kimura. "Bending loss of propagation modes in arbitrary-index profile optical fibers", *Applied Optics*, vol. 17, no. 10, pp. 1499–1506, 1978.

[8] J. D. Joannopoulos, R. D. Meade, and J. N. Winn. *Molding the flow of light.* Princeton University Press, 1995.

[9] J. Sakai. "Simplified bending loss formula for single-mode optical fibers", *Applied Optics*, vol. 18, no. 7, pp. 951–952, 1979.

Chapter 6

Conclusions

A wide range of modelling tools are available for modelling of PCFs in general. Which one to choose depends on the application of the results. The most common method for PCF-modelling is, as noted before, probably the plane wave method. It is a general approach which has many of features wanted in a modelling system, such as availability of highly optimised algorithms. It does, however, require that the fibre be repeated indefinitely. This requirement also applies to the standard localised function method — hence, both methods are limited to fibres with large cladding structures. Localised functions may be advantageous in situations where electromagnetic field coupling is to be considered, due to its representation of the fields in an orthonormal function set, with a comparatively low number of expansion coefficients. If leakage loss is to be considered, the multipole method is a better choice, which has the added feature of respecting the full symmetry of the structure and therefore does not introduce any erroneous, numerical birefringence, which may otherwise be encountered with other methods.

The purely Hermite Gaussian method, presented in this thesis, may be a candidate for optimisation calculations, of for instance a single hole-size, since the formulation of structures from superposition of defects in a background matrix. This allows altering a single air-hole, without the need for recalculating the whole structure. The straightforward formulation of the method also makes it particularly easy to set up a new structure from scratch. It is conceivable to take a SEM-micrograph of a fibre endface, find the positions and shapes of holes by means of automatic image processing, and calculate the properties of the fibre. For this vision to become reality, however it is necessary to lessen the strong dependence on the series characteristic width.

Our results for standard index guiding PCFs (triangular and square lattice fibres) show that the general features of index guiding fibres may be modelled using a formulation of this type, once an optimal characteristic width has been determined. In the triangular case we experienced a splitting of modes who should, by symmetry, be degenerate. This effect was not present in the quadratic lattice fibre, We concluded that this was due to the Cartesian expansion axes, used in the formulation of the model. Other notable results are dispersion characteristics for triangular fibres which agree with previously reported results.

The analysis of the pentagonal fibre (which although it is a mere generalisation of the triangular and quadratic lattice fibres, has, to the best of our knowledge, not been presented before), also exhibits mode splitting of degenerate modes similar to the case for the triangular fibre. This fibre has interesting effective area characteristics, increasing the mode effective area by up to 93% compared to the basic triangular fibre, for a moderate hole size, with no increase in core size. This may be of interest in applications demanding low nonlinear effects.

Localised function method are inherently not suited particularly suited for bandgap calculations, since the forced localisation inhibits the interaction of the electromagnetic fields with a large number of lattice periods. Furthermore, it is generally not an efficient procedure for bandgap calculations, since a large number of bands must be considered simultaneously when evaluating the effect of the characteristic width of the function series, in order to sort out unstable solutions. Nonetheless, we have shown that bandgaps may be identified in a honeycomb structure, and found them to support defect modes. The bandgap modes were found to have modal indices $\beta/k > 1$. Hence, the fields distributions did, as expected, not have their maximal field intensity in the central air-hole defect.

In some cases, such as the semi-periodic layered structures it is equally difficult to use other models, which are generally more suitable to bandgap calculations. In a plane wave formulation, the solutions associated with the hollow core would be obscured by solutions associated with the high-index voids inevitably appearing between supercells. This may be solved by inserting extra holes in the voids, but might also perturb the solutions. We have found localised stable solutions situated in a bandgap for two types of layered semi-periodic structures. These mode were truly air-guiding solutions (ratios of power in air: 73% and 84%).

Our calculations of microbend induced transition losses, lead us to the conclusion that index guiding PCFs may be designed to be less sensitive to such imperfections than step index fibres, on account of the comparatively large effective index contrast. It is necessary to keep in mind that the formulation only took overall bends into account, and did not include microdeformations of the fibre structure which inevitably will occur during the manufacturing process. We may, however, conclude the overall microbend induced transition losses are not the dominant cause of the higher losses found in low-loss index guiding PCFs ($\approx 1dB/km$), when

compared to commercial, low-loss step index fibres ($\approx 0.2dB/km$).

The spectral characteristics of macrobending loss in an air-guiding PCF, were investigated using an equivalent step index fibre approach, and predicted to have extremely steep loss-curve slopes: Within a wavelength range of $10nm$ the state of the bendloss is switched from full transmission to full radiation loss. On account of this verifying the results experimentally is predicted to be a difficult task.

6.1 Future work

Throughout the thesis, we have reminded ourselves of the dependence of solutions on the series characteristic width. It is our conclusion that, if the Hermite Gaussian method is to be useful beyond a few special cases, the dependence on this parameter *must* be reduced. Drawing on ideas from quantum chemistry, one way of reducing the dependency , could be to use several simultaneous expansion series, centred on sites (for instance on the centres of the inner ring holes) offset from the fibre centre. It is also conceivable to use simultaneous series of different characteristic width. Not that both of these strategies violate the the orthonormality of the function set. Hence, additional matrix operations would be needed in the formulation of the eigenvalue problem, which may be costly in terms of calculation time. It is our firm conclusion that future versions Hermite Gaussian method should include at least one of these solutions, regardless of the extra cost.

As noted, natural extensions to the formulation of microbend losses, include twists and bends in any direction. Bends may be formulated in any directions during calculation, in which case we may extend the curvature probability density function and the coupling coefficients into two dimensions, i.e. let fibre core displacement be determined by two stochastic processes, and use that as weight function for coupling coefficients. If the displacement processes may be considered independent the principle is straightforward. To consider twists, additional overlap integrals would have to be evaluated since coupling coefficients may no longer be expressed by summation over expansion coefficients.

With respect to macrobending loss investigations in air-guiding fibres it is our conclusion that further investigations need to take vectorial field effects into account to gain a more accurate description of the effect.

Acknowledgements

The author wishes to thank the following people for their help and support during the conception of this thesis. Without you it wouldn't have been possible. Thank you!

Anders Bjarklev, Jes Broeng
For kind supervision during these years.

Andrei Lavrinenko, Stig E. B. Libori, Morten G. Dyndgaard, Thomas Søndergaard, Thorkild Sørensen, Kristian G. Hougaard, Jesper Riishede, Theis P. Hansen
For fruitful discussions — scientific and otherwise.

Sofia Bergbäck
Bettina Petersen

List of publications

List of publications:

As a result of this Ph.D. project the following publications have arisen:

- J. Broeng, S. E. Barkou, A. Bjarklev, T. Søndergaard, E. Knudsen, "Review paper: Crystal fibre technology", *DOPS-NYT*, vol. 15, no. 2, pp. 22, 2000.

- E. Knudsen, J. Broeng, S. E. Barkou, A. Bjarklev, "Investigations of Photonic Crystal Fibers", *Photonic Crystals and Light Localisation in the 21st Century*, Hersonissou, Greece, jun., 2000.

- E. Knudsen, A. Bjarklev, J. Broeng, S. E. Barkou, "Macrobending loss estimation for air-guiding photonic crystal fibers",*14th international conference on Optical Fiber Sensors*, pp. 904, Venice, Italy, oct., 2000.

- T. Sørensen, J. Broeng, A. Bjarklev, E. Knudsen, S. E. B. Libori, "Macrobending loss properties of photonic crystal fibre", *Electronic Letters*, vol. 37, no. 5, pp. 287, 2001.

- T. P. Hansen, J. Broeng, S. E. B. Libori, E. Knudsen, A. Bjarklev, J. R. Jensen, H. Simonsen, "Highly Birefringent Index-Guiding Photonic Crystal Fibers", *Photonics Technology Letters*, vol. 13, no. 6, pp. 588, 2001.

- A. Bjarklev, J. Broeng, S. E. Barkou Libori, E. Knudsen, H. R. Simonsen, "Photonic crystal fiber modelling and applications",*Optical Fiber Communication Conference and Exhibit*, vol. 2, mar., 2001.

- A. Bjarklev, T. P. Hansen, K. Hougaard, S. B. Libori, E. Knudsen, J. Broeng, "Microbending in photonlic crystal fibres - an ultimate loss limit?",*27th European Conference on Optical Communication, 2001*, vol. 3, pp. 322, sep., 2001.

- T. Sørensen, J. Broeng, A. Bjarklev, E. Knudsen, S. E. B. Libori, H. Simonsen, J. R. Jensen, "Macrobending loss properties of photonic crystal fibres with different air filling fractions", *27th European Conference on Optical Communication*, vol. 3, pp. 380, sep., 2001.

- J. Riishede, S. E. B. Libori, A. Bjarklev, J. Broeng, E. Knudsen, "Photonic crystal fibres and effective index approaches", *27th European Conference on Optical Communication, 2001*, vol. 4, pp. 522, sep., 2001

- T. Sørensen, J. Broeng, A. Bjarklev, T. P. Hansen, E. Knudsen, S. E. B. Libori, H. Simonsen, J. R. Jensen, "Spectral Macro-bending Loss considerations on Photonic Crystal Fibres", *IEE Proceedings: Optoelectronics*, vol. 149, no. 5, pp. 206, 2002.

- K. G. Hougaard, A. Bjarklev, E. Knudsen, S. B. Libori, J. Riishede, P. M. W. Skovgaard, J. Broeng, "Coupling to photonic crystal fibers",*Optical Fiber Communication Conference and Exhibit*, vol. 6, pp. 627, 2002.

- E. Knudsen, A. Bjarklev, J. Broeng, S. E. B. Libori, "Modelling photonic crystal fibers with localised functions",*SPIE Photonics West 2002*, vol. 4616, pp. 81, San Jose, USA, jan., 2002.

- E. Knudsen "Modelling photonic crystal fibres with Hermite-Gaussian functions", *Optics Communications*, vol. 222, pp. 155, jul., 2003.

- E. Knudsen "Modelling of photonic crystal fibers with localized functions", *Journal of Optical and Fiber Communications Reports*, vol. 1, no. 3, 2004.

Patents:

- S. E. B. Libori, J. and Broeng, A. O. Bjarklev, C. Rasmussen and E. Knudsen, "Optical fibre for transmitting light, has improved polarization and dispersion properties, and includes micro-structured cladding region surrounding core region",
Patent numbers: WO200241050-A2,AU200223515-A, may, 2002.

- J. Broeng, P. M. W. Skovgaard, E. Knudsen, J. B. Jensen and M. D. Nielsen, "Optical waveguide for laser application, has cladding region surrounding core region and one-dimensional periodic structure of structural units with specific period, where core units has cross sectional elongated shape",
Patent numbers: WO2003100488-A, AU2003229545-A1., may, 2003.